4 Electromagnetic calorimetry

The Calorimeter Performance TDR [4-1] and the Liquid Argon Calorimeter TDR [4-2], submitted two years ago, gave a rather detailed description of the Electromagnetic (EM) Calorimetry of ATLAS and of its performance.

This chapter reviews the main issues related to the EM Calorimeter performance, obtained with the present (final) layout of the ATLAS detector. Emphasis will be put on progress and changes with respect to the Calorimeter TDR.

After a description of the present calorimeter layout, and in particular of the evolution since the Calorimeter TDR, the main progress in the simulation and reconstruction (more realistic description of the charge collection in liquid argon, improved simulation of the pile-up) are illustrated. The most important performance issues, and their impact on physics at the LHC, are then discussed: energy measurement, position and angular resolution, γ/π^0 separation, *etc*. The calorimeter performance was also evaluated by using complete physics events, namely $Z \rightarrow ee$ decays, which in addition represent a powerful tool for the *in situ* calibration of the calorimeter. The main outcomes of these studies are described. Finally, preliminary results obtained from the beam tests of the EM Calorimeter 'module zero' are presented.

4.1 Present detector layout

An overall view of the EM Calorimetry is shown in Figure 4-i and a brief description can be found in Chapter 1. Since the Calorimeter TDR, nothing has changed in design concept. However, due to various constraints, such as cost and engineering issues, or as a result of additional studies, a few elements have changed or evolved. The main changes are described briefly in this section.

Module zero's of the barrel presampler (PS), barrel EM calorimeter and end-cap EM calorimeter have been built and partially tested with beam. Experience from the assembly of the modules has also been used to simplify the construction and define Quality Control procedures. A few selected measurements made on some parts of the calorimeter already delivered are presented in Section 4.3.6, since they have an impact on the uniformity of the calorimeter response.

4.1.1 Changes in the barrel cryostat

4.1.1.1 Inner cold wall and bulkheads

In the Liquid Argon Calorimeter TDR, the barrel cryostat had an inner cold wall with a so-called 'isogrid' structure. The same structure was also proposed for the smaller radius part of both the cold bulkhead and the warm bulkhead, in order to reduce dead material in the transition region between barrel and end-caps. While isogrid is a technique mastered by a few companies, it was realised that large size tests would have been necessary in order to validate the most critical parts, namely the cylinder to bulkhead transitions. It appeared also that those transitions areas would have had to be rather massive, thus partly reducing the advantages of the technique. An alternative study was therefore undertaken, based on a much simpler plain tapered cold wall. By adding a reinforcement ring in the symmetry plane, a cold wall with a thick-

ness between 28 mm (η=0.2) and 14 mm (η=1.2) was found to meet the safety requirements (the main constraint is given by buckling). As shown in Table 4-1, this solution increases the amount of material in front of the EM Calorimeter by 0.25 X_0 with respect to the isogrid at small pseudorapidity, where the overall material budget is not critical, and by only 0.1 X_0 at large pseudorapidity, where the total material in front of the calorimeter is more critical. Furthermore a solid cold wall has the advantage of a more uniform material distribution than the isogrid structure. The impact of this wall change on the EM Calorimeter performance is marginal, as discussed in more detail in Section 4.3. The cold bulkhead and the flange connecting the bulkhead and the cold wall have also been studied in detail, and their thickness minimised. This flange is now located on 'side C' of the detector ($z < 0$). Furthermore, in order to reduce the material in front of the end-cap calorimeter, the bolts connecting the inner warm cylinder to the warm bulkhead are now made of aluminium.

4.1.1.2 Supporting structure

In the design presented in the Liquid Argon Calorimeter TDR, the cold vessel (which contains the calorimeter and the liquid argon) was supported by two steel slings at each end. It was realised that, due to the difference in expansion coefficients between aluminium and steel, some extra space would have been necessary to accommodate a small vertical excursion between the solenoid (attached to the warm vessel) and the cold vessel. Fitting the sling ends in the warm bulkhead while preserving the symmetric distribution of feedthroughs around the circumference turned out to be quite difficult as well. In order to circumvent these difficulties, a different system of supporting, based on feet, has been implemented.

4.1.1.3 Cooling

The heat brought in at the feedthrough level by conduction in the cables is about 500 W per side. While this is a sizeable fraction (about 50%) of the total heat input, the heat exchangers were laid on the inner surface of the outer cold vessel, far from the feedthroughs. Such a layout was not optimal for limiting temperature variations in the calorimeter to a fraction of a degree, which is needed for a response uniform to a fraction of a percent. Therefore it has been decided to add, at each end of the cold vessel, a cooling loop near the feedthroughs. It is laid against the cold bulkhead, at the largest possible radius. Calculations of temperature uniformity, incorporating this new feature, have been recently started using a 3D model.

Table 4-1 Thickness of the old isogrid wall and of the new tapered wall, as a function of pseudorapidity, as seen by a particle coming from the interaction vertex.

Pseudorapidity	Thickness of isogrid wall (X_0)	Thickness of tapered wall (X_0)
0.24	0.12	0.37
0.64	0.14	0.37
1.0	0.17	0.37
1.2	0.21	0.36
1.3	0.23	0.37
1.4	0.25	0.35

4.1.2 Changes in the end-cap cryostat

A few changes have taken place in the end-cap cryostat design, mainly in order to improve the reliability and to reduce the cost of fabrication. Among the main points are an improved design of the feet, and the choice of double cold seals. None of these changes affect the performance of the EM Calorimeter. It should also be noted that the space reserved for the beam-pipe pumps in front of the FCAL is now likely to stay empty. This will improve the background situation in the FCAL, but has almost no visible effect on the performance of the EM Calorimeter. Furthermore, due to a different ganging scheme of rod-shaped electrodes in the FCAL (see Chapter 5), the number of feedthroughs per end-cap was reduced from 28 to 25. Finally the cold door in the back (in aluminium) is now somewhat thicker (+50 mm), at the expense of space for cables and of the copper plug which is now thinner (-30 mm). The induced change in background in the chambers of the Muon System is negligible.

4.1.3 Improvements in the optimal filtering

In the course of the development of the front-end readout boards, and using measurements made in test beams, it was found that the merits and limitations of the 'optimal filtering' technique needed to be reanalysed. This study [4-3] was started because, by using five samples and optimising the signal to noise ratio for test-beam data, it was not possible to obtain the gain factor on electronic noise which was anticipated. The analysis showed that the main limitation comes from an 'aliasing effect': with a sampling period of 25 ns, components of the noise frequency spectrum around 40 MHz, 80 MHz, *etc.* are fully transmitted, and contribute sizably to the noise after sampling. As a result of this work, which included the full description of the preamplifiers and shapers already prototyped for ATLAS, the electronic and pile-up noise as a function of luminosity as well as the time constant of the shaper have been reanalysed. Figure 4-1 shows that, with a time constant of 15 ns (instead of 13 ns as in the Liquid-Argon Calorimeter TDR), optimal filtering allows minimisation of the total noise for luminosities between 10^{33} $cm^{-2}s^{-1}$ and $5x10^{34}$ cm^{-2} s^{-1} as efficiently as changing by hardware the time constant (15 ns) selected for the nominal high luminosity of 10^{34} $cm^{-2}s^{-1}$. Going beyond this luminosity range in an optimised way would require changing the shaper time constant. The feasibility of such a scheme for the very low luminosity case (LHC start-up, heavy-ion running) is under study. More details on pile-up and electronic noise are given in Section 4.2.4.

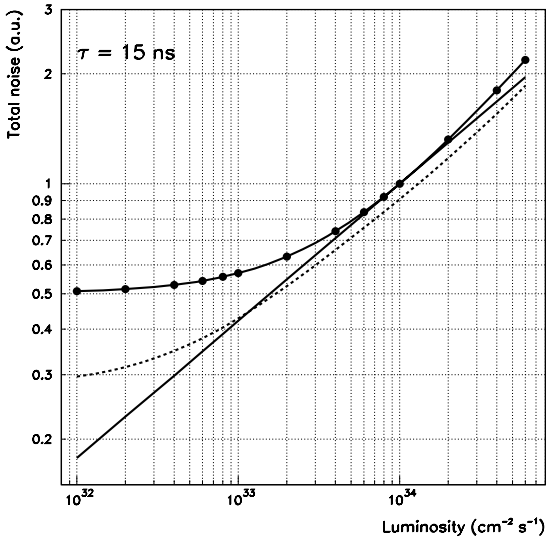

Figure 4-1 Total noise as a function of luminosity for a shaping constant of 15 ns. The dots and the dashed line show the performance without and with optimal filtering respectively. The full line indicates the total noise which could be obtained with the best possible (hardware) time constant for each luminosity.

4.2 Simulation and reconstruction environment

The ATLAS simulation and reconstruction environment is described in Chapter 2. Therefore only aspects related to the EM Calorimeter are discussed here.

The GEANT simulation of the EM Calorimeter did not change significantly since the Calorimeter TDR. It includes all details of the accordion geometry and of the cryostats, as well as a faithful description of the inactive material (cables, services, inactive liquid, *etc.*), as shown in Figure 4-i. The recent changes in the cryostat design mentioned in Sections 4.1.1 and 4.1.2 have been implemented in the simulation.

Very recently, a better simulation of the charge collection in the liquid-argon gaps based on realistic field maps has been developed. This is discussed in Sections 4.2.1 and 4.2.2. This detailed simulation has allowed evaluation of the impact of a realistic charge collection mechanism on several performance issues. It was found that the impact is negligible in most cases (see Section 4.3), therefore most of the results shown here were obtained without the full charge collection mechanism.

4.2.1 Signal simulation in the barrel

In the simulation used for the Calorimeter TDR, the signal collection in the barrel used the energy deposited in the liquid argon. This ignores the drifting of the ionisation charges in an electric field with large non-uniformities in the accordion folds. The total current induced by a charge q drifting in the gap is expressed by:

$$i = q\bar{v}(\bar{E}/V)$$

where $\bar{E}$ is the local electric field, $\bar{v}$ is the drift velocity depending on E as $\sim E^{0.3}$ and V is the voltage applied between electrodes.

In the straight parts, *i.e.* regions with plane and parallel electrodes, the electric field is uniform ($E \sim 10$ kV/cm). In the folds, which represent about one third of the barrel active volume, the two-dimensional electric field is determined by a numerical solution of Poisson's equation (PRIAM package [4-4]).

To get the resulting induced current, each hit in the liquid argon (from GEANT) is divided into n quasi-punctual charges ($<n> \sim 7$) of 200 μm length (below this value no change in results was observed). Each elementary charge drifts in the local electric field. The resulting current (see equation above) is then folded with the specific electronic functions (impulse response of the preamplifier-shaper chain), which depend on both the longitudinal compartment and the η coordinate of the hit. In the straight parts, the uniform field yields a constant current during the drift time and the convolution with the electronic function is straightforward. In the folds, on the other hand, the drifting of an elementary charge has to be followed step by step in time (typical time step: ~2 ns) up to about 100 ns. The resulting current $i(t)$ is then folded with the corresponding electronic function. The increase in the event processing time using this method (including the response of the electronic chain) instead of deposited energies is about 10%.

Improvements have also been made in the description of the signal sharing between adjacent strips. Due to the fine granularity in η of the first compartment of the EM Calorimeter, an elementary charge induces a signal on more than one strip (typically three strips are involved). To take this sharing into account, in the Calorimeter TDR simulation the total charge (not the total

current) induced on a semi-infinite conducting plane bounded by a straight line had been used. Because of the non-uniformity of the electric field in the folds, the total current induced by an elementary charge in the first compartment is obtained as explained above, then sharing functions between the hit strip (under the charge) and the two neighbour strips are used. These functions depend on two variables: the distance from the charge to the electrode (divided by the local gap width), and the distance from the charge to the strip middle (divided by the local strip width). Pile-up (if any) due to multiple elementary charges is taken into account.

4.2.2 Signal simulation in the end-cap

In the end-cap calorimeter the gap geometry varies with radius. Therefore a simulation based on the energy deposited in the liquid argon is not fully realistic, because the electric field varies significantly with radius even in the straight parts of the electrodes. Charge collection effects in the end-cap are important, and are now simulated in two steps.

In the straight parts of the electrodes, the signal (S) is calculated using the expression

$$S = (E/g(R))R^{1.3}$$

where E is the deposited energy and $g(R)$ the gap thickness as a function of radius. It is obtained from the current expression given in the previous Section, by taking into account the fact that the electric field is $E=V/g$ and that the drift velocity v is proportional to $E^{0.3}$. The gap thickness at each radius is obtained from a linear interpolation based on a precalculated table. The high-voltage variation with pseudorapidity is taken into account during analysis.

On the other hand in the folds, where the electric field is not uniform, electric field maps are calculated using the PRIAM package. As in the barrel, each GEANT hit is divided into several punctual charges and for each of them the contribution to the current is calculated. Since the geometry of the end-cap is more complicated, the procedure for calculation of the current has been simplified with respect to that in the barrel: the current is assumed to be proportional to the electric field at the position of the elementary charge, without convoluting with the exact shaping function. For small shaping time this simplification has no significant impact.

4.2.3 Reconstruction in the EM Calorimeter

The reconstruction in the EM Calorimeter is divided into four steps.

The deposited energies (DIGI's from GEANT) are stored into cell matrices, with one matrix per region of uniform granularity. Electronic noise and pile-up can be added at this level by using the method described in Section 4.2.4. Five samples can be made available and digital filtering can be applied. The energies in all matrices are then calibrated, on a cell-by-cell basis, by asking that the total energy reconstructed in the calorimeter for photons of E_T = 50 GeV be equal, on average, to the incident energy.

The energies are then mapped onto a matrix of granularity $\Delta\eta x\Delta\phi = 0.025x0.025$ and summed in depth. A sliding window algorithm with a 5x5 cell window is applied on this matrix. The threshold on the cluster energy can be chosen as a function of luminosity, and may depend on the physics channel. Figure 4-2 shows the number of fake clusters, in the 5x5 window, due to electronic noise and pile-up at high luminosity for various cluster thresholds.

Around the direction of each cluster, the energies are measured in each compartment in windows of various sizes. The energies are corrected for the η and ϕ modulations (see Section 4.3.3) and the calibration is adjusted to take into account the finite cluster size. The ϕ position is measured in the middle compartment and corrected for an offset due to the accordion shape of the cells. The η positions are measured in the first two longitudinal compartments. They are corrected for the 'S-shapes' (see Section 4.4.2), and they are then used to determine the shower direction and the position of the primary vertex in z.

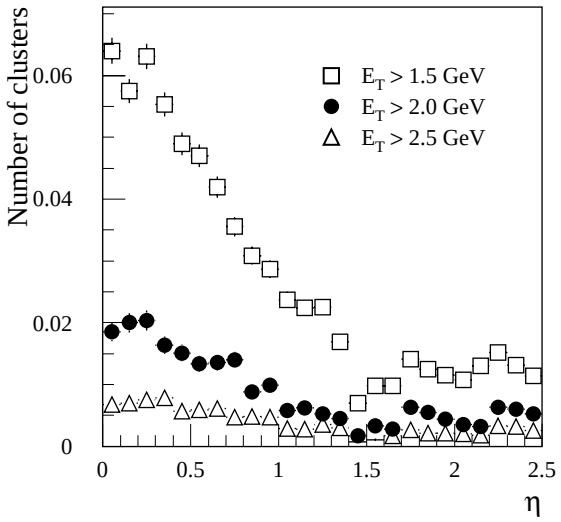

Figure 4-2 Number of fake clusters due to pile-up and electronic noise in a window of size $\Delta\eta x\Delta\phi = 0.125x0.125$, as a function of pseudorapidity for different cluster thresholds.

Finally, an efficient electromagnetic shower identification algorithm, based only on the information from the Hadronic and Electromagnetic calorimeters, is used. It provides an efficiency for electrons and photons of $E_T = 20$ GeV, integrated over $|\eta| < 2.4$ but excluding the barrel/end-cap transition region, of larger than 96%, while keeping less than 2% of single charged pions. More powerful electron and photon identification requires the use of the Inner Detector and is described in Chapter 7.

4.2.4 Simulation of pile-up and electronic noise

As discussed in Section 2.3.1, 24 minimum-bias events (around 3500 particles inside $|\eta| < 5.0$) are produced on average for each bunch crossing when running at high luminosity. To cope with this environment, the EM Calorimeter is read out using fast bipolar shapers with a peaking time of ~35 ns. The simulation of the pile-up in the EM Calorimeter is described in some detail in Section 2.3.3. The electronic noise with the correct time correlations is superimposed to the energies stored in the individual cells just before reconstruction. The digital filtering procedure may also be used in this more refined simulation procedure. In this way, the electronic shaping can be modified (within limits) to reduce the electronic noise for operation at low luminosity.

Figure 4-3 shows the energy spectrum of the pile-up expected at high luminosity in the middle compartment of the EM Calorimeter for a typical cluster size of 3×7 cells in $\eta x\phi$. The correlation between the pile-up noise and the bunch-crossing number is illustrated in Figure 4-4: large positive fluctuations are always caused by the so-called 'in-time pile-up', *i.e.* events sampled at the peak of the shaper response.

4.2.4.1 Pile–up levels in the EM Calorimeter

The results presented here are based on 5000 fully-simulated minimum-bias events. The rms of the pile-up transverse energy distribution is shown in Figure 4-5 for different cluster sizes and separately for the presampler, the strip section and the middle compartment of the EM Calorimeter. The presampler energy was weighted as described in Section 4.3.2. The increase (decrease) of the pile-up in the presampler (calorimeter) at the transition between the barrel and the end-

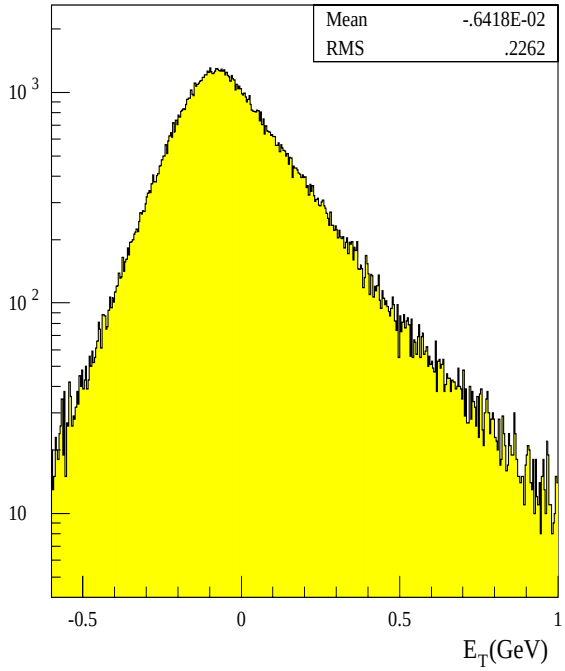

Figure 4-3 Distribution of the pile-up transverse energy in a 3×7 cell cluster in the middle compartment of the EM Calorimeter at η = 0.3.

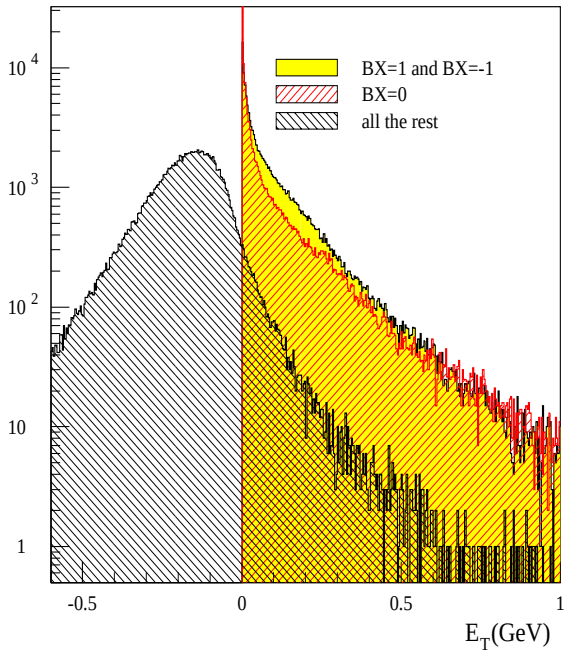

Figure 4-4 Different contributions to the pile-up transverse energy in a 3×7 cell cluster in the middle compartment. BX=0 denotes the pile-up at bunch crossing zero, that is the in-time pile-up; BX = 1 and BX = -1 refer to events delayed by ±25 ns with respect to the peak, *i.e.* belonging to the previous and next bunch crossing.

cap calorimeter is due to the large amount of upstream material, which absorbs soft particles traversing these regions, so that they reach the presampler but not the calorimeter. Figure 4-6 shows the total noise (electronic plus pile-up) summed over the presampler and the first two longitudinal compartments of the calorimeter, as well as the electronic noise alone. The cluster sizes are 3x5, 3x7, and 5x5 cells (units of $\Delta\eta\times\Delta\phi = 0.025\times0.025$) in the middle compartment, and respectively 1×1, 1×2, and 2×2 in the strips and in the presampler (units of $\Delta\eta\times\Delta\phi = 0.025\times0.1$). The pile-up levels obtained with the present more realistic simulation are similar to those reported in the Calorimeter Performance TDR.

The occupancy of the EM Calorimeter is presented in Figure 4-7, which shows the fraction of cells where the pile–up energy exceeds a given threshold expressed in units of electronic noise at high luminosity. At high luminosity the fraction of cells with a pile-up energy exceeding two standard deviations of the electronic noise is about 1% in the barrel and less than 10% in the end-cap.

4.2.4.2 Coherent noise

Since the EM Calorimeter has almost 200 000 channels, the presence of coherent noise, which scales linearly with the number of channels, could have a serious impact on measurements involving many cells, such as the measurement of the event missing transverse energy. According

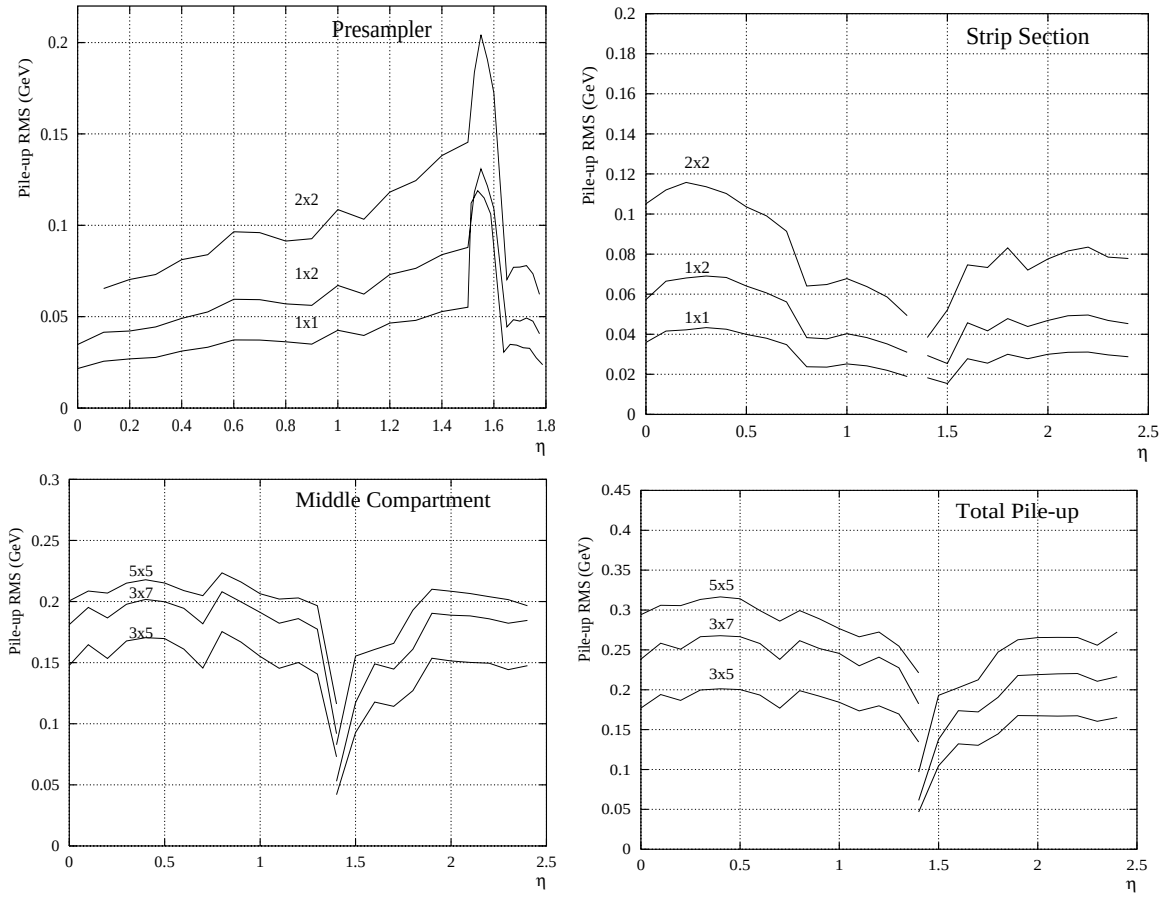

Figure 4-5 The rms of the pile-up transverse energy distribution as a function of pseudorapidity in the presampler, the strip section, the middle compartment and the total. Three different cluster sizes are shown: 3x5, 3x7 and 5x5 for the middle compartment (units of $\Delta\eta x\Delta\phi$ = 0.025x0.025), and 1x1, 1x2 and 2x2 for the strip section and the presampler (units of $\Delta\eta x\Delta\phi$ = 0.025x0.1) respectively. In the top left plot, the contribution of the scintillator has been included in the region $1.5 < \eta < 1.6$.

to studies reported in [4-1], the coherent noise in the middle compartment of the EM Calorimeter should not exceed 3 MeV per channel, which is about 5% of the white noise, in order not to spoil the E_T^{miss} measurement.

The coherent noise can be controlled by a careful design of the grounding and shielding on the input stages. Thus, the preamplifiers are located very close to the feedthroughs, inside a Faraday cage which comprises the cryostat, the feedthroughs and the crates. This minimises the sensitivity to external electromagnetic interferences. The ground currents are minimised by an optical coupling of the readout boards to the external world for fast digital input/output, by avoiding large ground loops and by providing low-impedance connection to the crates. Application of these criteria, except for the optical coupling, to the module-zero tests of '98, reduced the coherent noise to the level of 10% of the white noise over 128 channels. Furthermore, bench tests with optical coupling has decreased this value to 5%, which is within the specifications mentioned above.

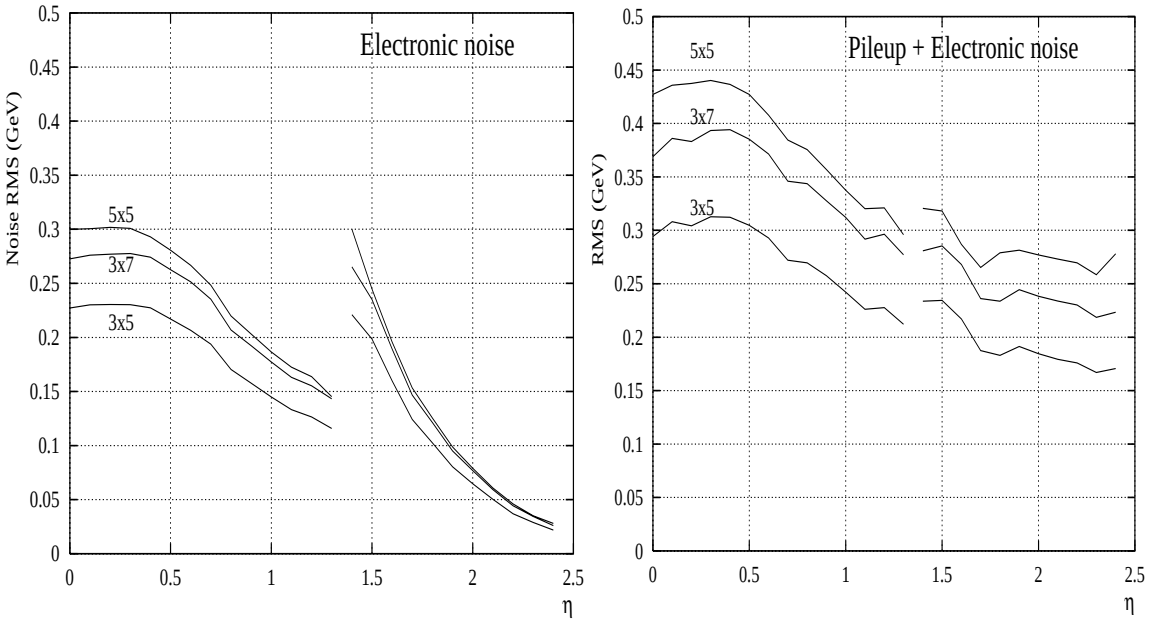

Figure 4-6 The rms of the electronic noise (left) and total noise (right) transverse energy distributions, as a function of pseudorapidity, for three different clusters (see text).

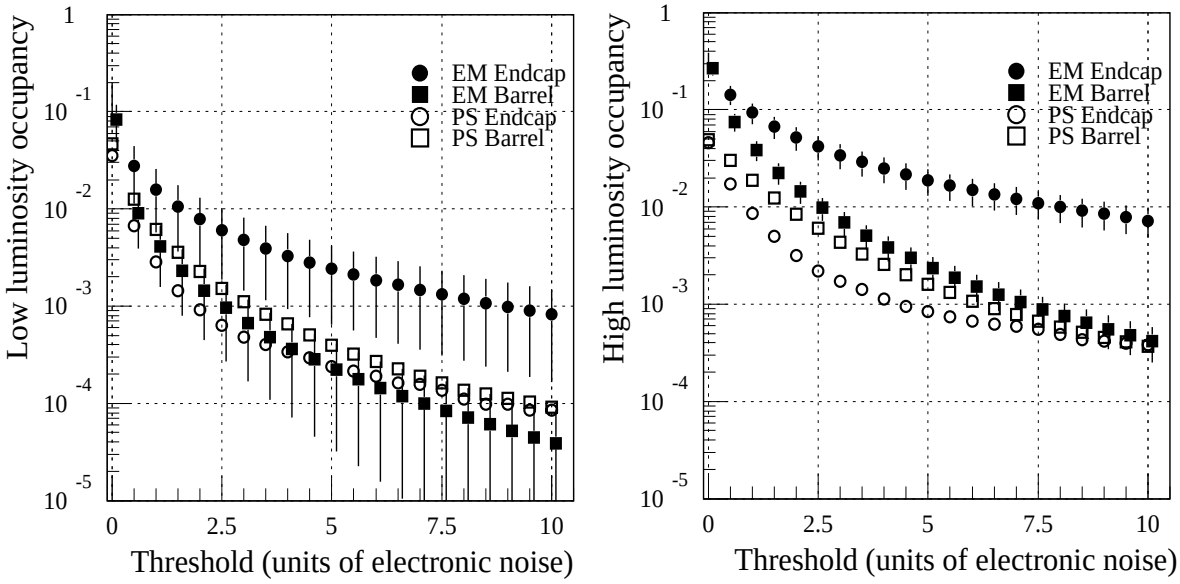

Figure 4-7 The average fraction of cells with a pile-up energy larger than a given energy threshold (in units of electronic noise), as a function of the threshold, at low (left) and high (right) luminosity.

4.3 Energy measurement

The procedure to reconstruct the energy of an incident particle in the EM Calorimeter has been described in detail in [4-1]. Therefore only the main features will be recalled here.

In general, the reconstructed energy can be written as:

$$E_{tot} = w_{glob}(w_{ps}E_{ps} + E_{str} + E_{mid} + E_{back}) \quad \text{4-1}$$

where w_{glob} is a global calibration factor, and E_{ps}, E_{str}, E_{mid} and E_{back} are the energies measured in a given cluster of cells in the presampler, strip section, middle and back compartments of the calorimeter respectively. The presampler weight w_{ps} is chosen to optimise the energy resolution. The energy response of the calorimeter is potentially affected by several factors which are described one by one in the following sections, after a discussion of the cluster size.

4.3.1 Optimisation of the cluster size

The optimum cluster size is the result of a compromise between two competing effects. A relatively large cluster is needed to fully contain the shower and therefore to limit the impact of lateral fluctuations on the energy resolution. On the other hand, the smallest possible cluster is needed to reduce the contribution of the pile-up and electronic noise to the energy resolution. The cluster size depends on the particle type, energy and pseudorapidity. Electron reconstruction needs larger clusters than photons because of their larger interaction probability in the upstream material and the presence of a magnetic field.

The results presented in the Calorimeter Performance TDR, which were obtained with a pile-up approximately simulated by a simple Gaussian smearing of the energy deposited in each cell, were checked using the complete simulation of the electronic and pile-up noise described in Section 4.2.4.

In the strip section, the optimal cluster size was obtained by looking at the rms of the energy measured inside a cluster of increasing width in η divided, event by event, by the total energy in the first compartment. In azimuth, an average size of 1.5 strips was used, that is one or two strips were chosen according to the shower position with respect to the strip centre. As an example, Figure 4-8 shows the results obtained for electrons of E_T = 20 GeV at η = 0.9. In the presence of electronic and pile-up noise, a shallow minimum can be seen around ±8 strips (with respect to the shower impact point), in agreement with the result presented in [4-1].

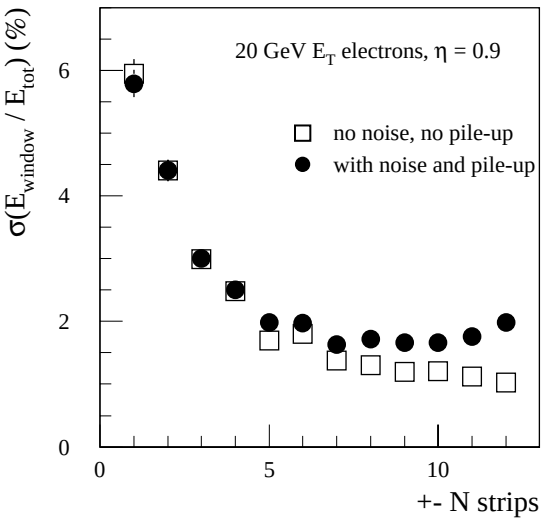

Figure 4-8 Rms of the energy deposited in ±*N* strips around the electron impact point, divided by the total energy in the strip section without noise and pile-up, for electrons of E_T = 20 GeV at η = 0.9, as a function of the number of strips used.

The optimal cluster sizes in the middle compartment of the barrel calorimeter were found to be the same as in [4-1], *i.e.* 3x5 cells in ηxφ for unconverted photons and 3x7 cells for electrons and converted photons. In the end-caps, where the cell size in η is smaller with respect to the shower size than in the barrel, and where the effect of the magnetic field in φ is also smaller, a window of 5x5 cells gives the best performance. For example, for unconverted photons of E_T = 50 GeV at η = 1.8, the rms of the energy deposited in windows of 3x5, 3x7 and 5x5 cells, divided by the total energy in the middle compartment, is (0.738 ± 0.018)%, 0.670% and 0.585% respectively.

For low-energy particles, the fraction of the shower energy deposited in the back compartment of the calorimeter is small: on average 2.7% of the particle energy for electrons of 50 GeV at $\eta = 0.3$. Therefore, because of the contribution of the electronic noise, it is better not to use the energy measured in this compartment at low energy. Table 4-2 shows the calorimeter energy resolution obtained with and without including the energy measured in the back compartment, when the electronic noise and the pile-up are added. It can be seen that the energy resolution for particles with energy smaller than 50 GeV is slightly better if the back compartment is not used. At higher energies, on the other hand, the energy deposited in the back compartment must be included (see Section 4.3.4).

Table 4-2 Energy resolution of the EM Calorimeter for electrons of various energies at $\eta = 0.3$, obtained by using or not using the energy measured in the back compartment.

	E = 10 GeV	**E = 50 GeV**	**E = 200 GeV**
With back compartment	$(6.33 \pm 0.09)\%$	$(1.39 \pm 0.02)\%$	$(0.795 \pm 0.018)\%$
Without back compartment	$(6.24 \pm 0.09)\%$	$(1.38 \pm 0.02)\%$	$(0.847 \pm 0.021)\%$

The optimal cluster size in the presampler was chosen by looking at the variation of the calorimeter energy resolution as a function of the number of presampler cells used. As a result, a window of size 2x1.5 presampler cells (1.5 means that one or two cells are used in ϕ, according to the shower position with respect to the cell centre) was used for converted photons and electrons, and a window of size 2x1 cells was used for unconverted photons.

At low luminosity, somewhat larger cluster sizes could be used, since the total noise is a factor of two smaller than at high luminosity (see Figure 4-1). However, for the study presented here the cluster sizes determined at high luminosity as described above were used in all cases. Therefore the low-luminosity results are slightly conservative.

4.3.2 Impact of dead material

The material in front of the EM Calorimeter is shown in Figure 4-ii, and a comparison with the layout described in [4-1] is presented in Figure 4-9. The total amount has increased since the Calorimeter Performance TDR due to:

- The use of a solid cold wall for the barrel cryostat. The increase in material is significant only at small pseudorapidity thanks to the tapered shape.
- A 10% increase in the thickness of the Pixel and SCT layers (see Chapter 3). Since these layers are at small radii, they have a significant impact on the energy reconstructed in the calorimeter, in particular on the appearance of low-energy tails.
- A more realistic description of the Inner Detector services, which contribute for $0.7 < |\eta| < 1.8$ and in front of the end-cap inner wheel (Figure 4-9). The services, however, are located at relatively large radii and therefore their impact on the calorimeter performance is small in most cases.

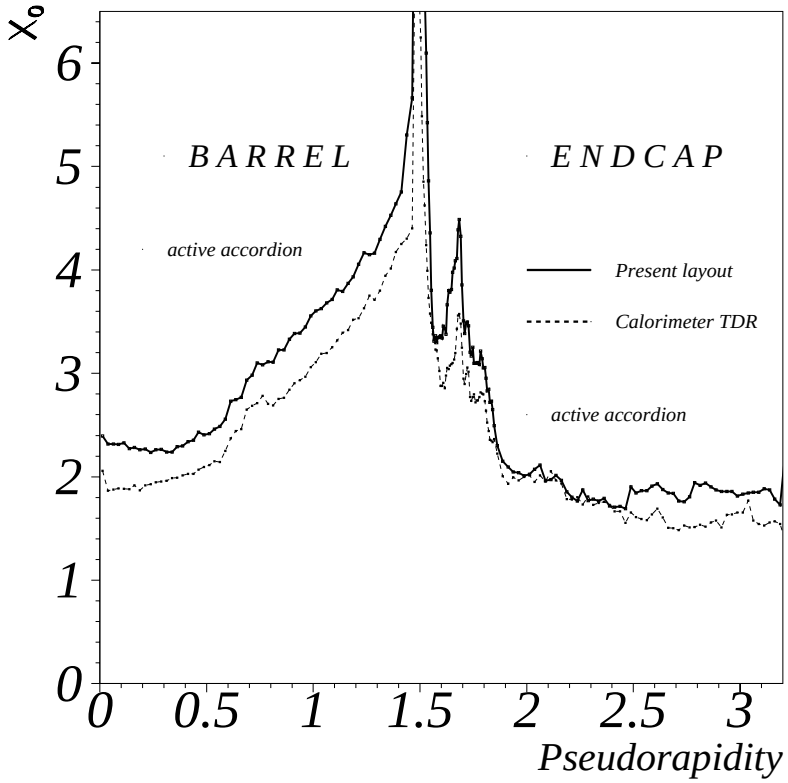

Figure 4-9 Amount of material in front of the EM Calorimeter, as a function of pseudorapidity, with the layout described in [4-1] and with the present layout.

On the other hand, the increase in the region $|\eta| \sim 1.7$ is due to the fact that, in the detector simulation used for the studies presented here, the bolts of the warm flange were in titanium instead of aluminium. No significant material increase is expected with aluminium bolts.

As already discussed in [4-1], the material in the Inner Detector, at large distance from the EM Calorimeter and inside a magnetic field, mainly contributes to the formation of low-energy tails in the energy spectra reconstructed in the calorimeter, whereas the material close to the calorimeter (cryostat, coil) broadens the width of the Gaussian part of the spectra. In both cases the effect is more serious for lower energies and for electrons rather than for photons. The low-energy tails are discussed in Section 4.3.7.

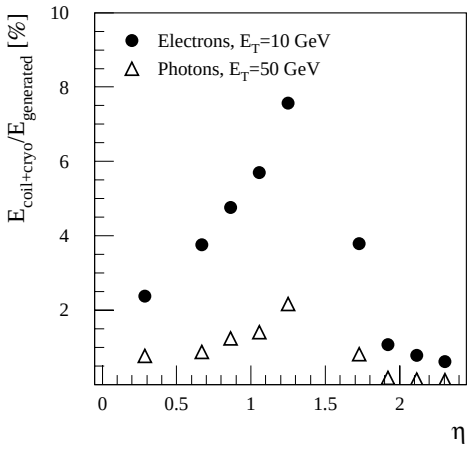

Figure 4-10 Fraction of energy lost by electrons and photons in the cryostats and coil as a function of pseudorapidity.

The transition between the barrel and the end-cap calorimeter represents a special case, because there the amount of material in front of the calorimeter reaches several radiation lengths. Dedicated devices (end-cap presampler, scintillator slab) are used in order to limit the impact of this material on the calorimeter energy measurement. Details about the layout and the calorimeter response in this region are discussed in Section 4.3.8.1.

The fraction of energy lost by electrons of E_T = 10 GeV and photons of E_T = 50 GeV in the cryostat and coil is shown in Figure 4-10 as a function of pseudorapidity. As already mentioned, the losses are larger for low-energy electrons than for high-energy photons. The shape of the distribution in Figure 4-10 reflects the material profile in front of the calorimeter (see Figure 4-ii).

The energy losses can be recovered, and thus the resolution improved, by weighting the energy deposited in the presampler. The optimisation of the weight (w_{ps} in Equation 4-1) was performed for electrons and for converted and unconverted photons of various transverse energies and at different incidence points. The calorimeter energy resolution was studied for several presampler weights, and the weight which minimises the resolution was determined. An example is shown in Figure 4-13, which demonstrates that the use of the presampler improves the calorimeter energy resolution significantly. The optimum weight was found to be $w_{ps} \sim 3.5$ in the barrel. The linearity of the calorimeter response, which is better than 1%, is not affected by the presampler weighting .

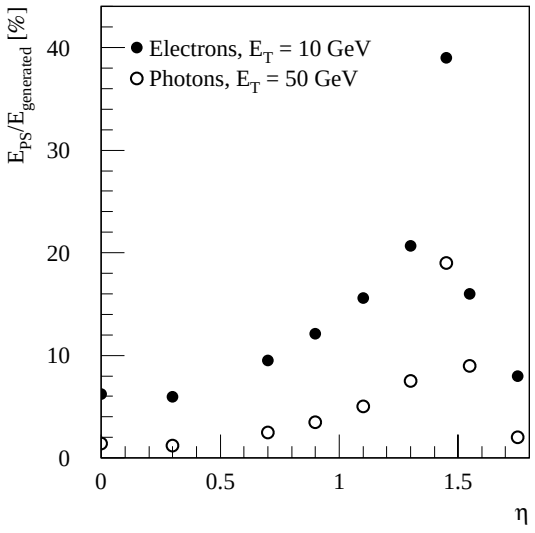

Figure 4-11 Fraction of energy in the presampler (after weighting) for electrons of E_T = 10 GeV and photons of E_T = 50 GeV, as a function of pseudorapidity.

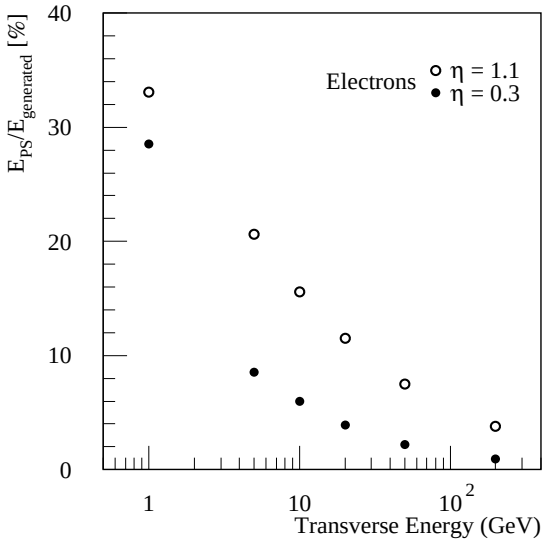

Figure 4-12 Fraction of (weighted) energy in the presampler for electrons incident at two pseudorapidities, as a function of the electron energy.

The impact of the presampler on the calorimeter energy measurement is also illustrated in Figure 4-14, which shows the energy spectra for electrons of E_T = 10 GeV at η = 1.3 obtained using and without using the presampler information.

The role of the presampler [4-5], *i.e.* to ensure robustness against possible increases in the amount of material in front of the calorimeter, has been recently demonstrated with the increase in the thickness of the barrel cold wall: essentially no degradation is observed in the energy res-

olution with respect to the isogrid solution, as discussed in Section 4.3.5. The weighted energy in the presampler is shown in Figures 4-11 and 4-12 as a function of pseudorapidity and energy and for electrons and photons.

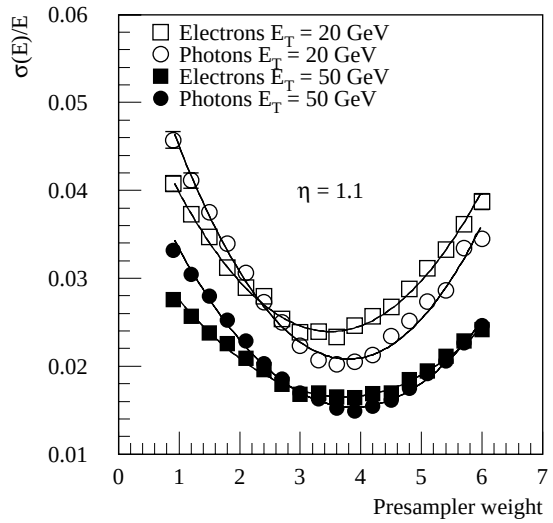

Figure 4-13 Energy resolution of the EM Calorimeter (a large cluster size is used) as a function of the presampler weight for electrons and photons of E_T = 20 GeV and 50 GeV at η = 1.1.

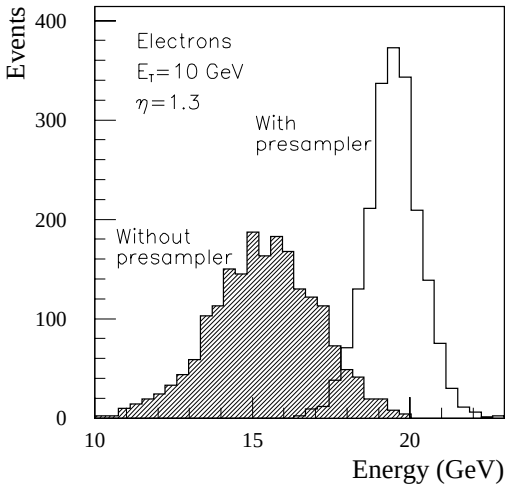

Figure 4-14 Energy spectra reconstructed in the EM Calorimeter with (white histogram) and without (black histogram) using the presampler information for electrons of energy 19 GeV at η = 1.3. Both histograms are normalised to the same number of entries.

4.3.3 Variation of response with φ and η

Due to the accordion geometry (imperfect overlap among absorbers due to the finite bending radius), the amount of passive material crossed by an incident particle varies as a function of the position in φ. This gives rise to a response modulation, called 'φ-modulation'. The geometrical parameters of the accordion, such as the length of the folds and the bend angle, have been optimised, as a function of the calorimeter depth, so as to minimise this response variation.

The energy reconstructed in the calorimeter as a function of φ is shown in Figure 4-15 at several pseudorapidity points in the barrel and end-cap.

In the barrel, the response variation has an rms of 0.35% before correction. In the end-cap, due to the more complicated geometry, the absorber overlap is less good, and the response rms is 0.6%. The φ-modulation can be corrected for with a function (superimposed to the calorimeter response in Figure 4-15), consisting of the sum of four sigmoids. The parameters of the sigmoids depend on the pseudorapidity. After correction, the residual rms is 0.2-0.3%.

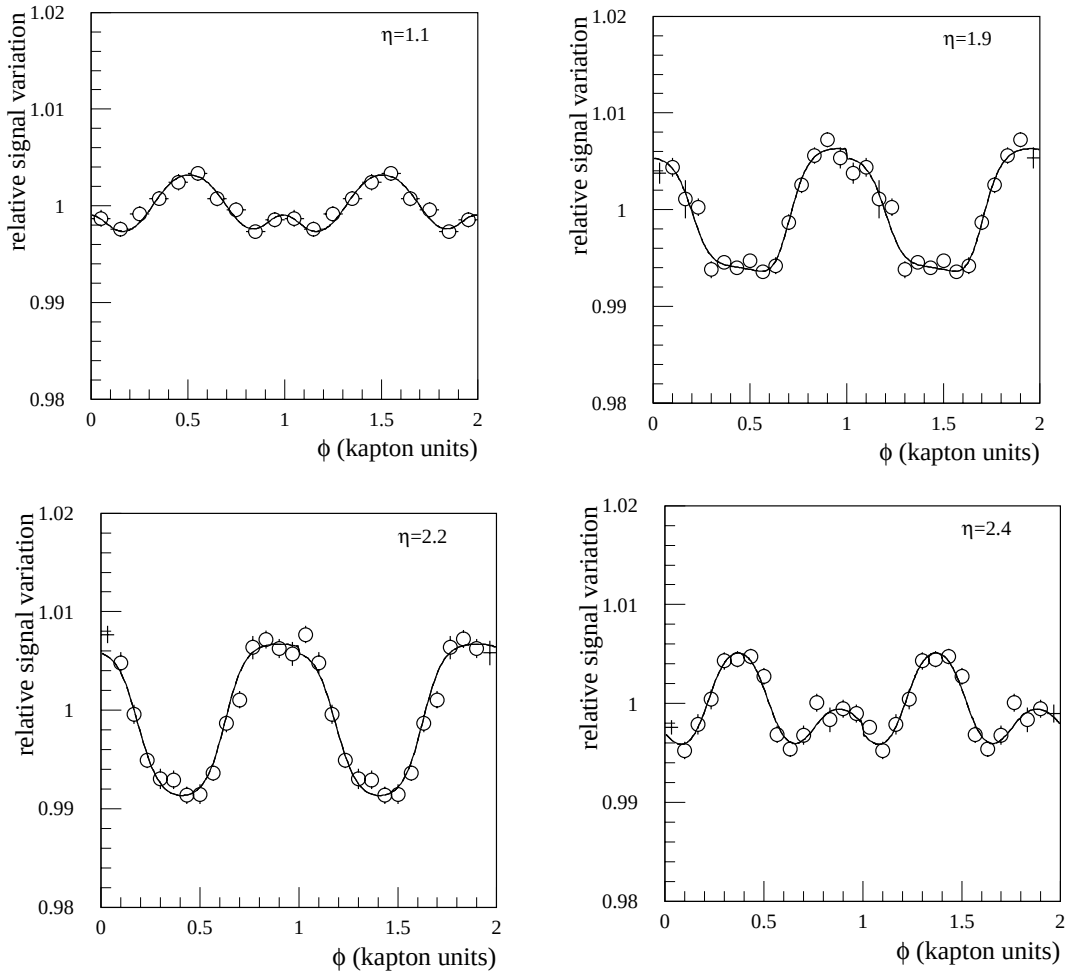

Figure 4-15 Calorimeter response to photons of E_T = 50 GeV, normalised to the generated energy, as a function of ϕ inside one cell, as obtained at various pseudorapidity points: η = 1.1 (top left), η = 1.9 (top right), η = 2.2. (bottom left), η = 2.4 (bottom right). The correction function is superimposed. One Kapton unit corresponds to 1/4 of a cell in the barrel and 1/3 in the end-cap.

The response modulation in ϕ is affected by the non-uniformity of the electric field in the accordion folds. Figure 4-16 shows the calorimeter response in the end-cap, as a function of ϕ, as obtained when the realistic field map described in Section 4.2.2 is used. It is compared to the response obtained with a uniform electric field, as used in the baseline simulation code. With a realistic field, the modulation is less regular and has a smaller amplitude. This is because the peaks in the response, which are due to the excess of liquid in the accordion folds, are to some extent compensated by the lower electric field in the folds.

The cluster size used for the energy measurement is relatively small in η (three cells in most cases). Therefore, the shower energy is not fully contained, and the calorimeter response depends on the particle impact point inside a cell: the response is maximum for particles hitting the cell centre, and drops (by typically 5%) at the cell edges. This response variation is corrected for with a second-order polynomial function, by using the shower position reconstructed by the calorimeter itself. The parameters of the η–correction depends on the pseudorapidity, since the physical size of the cells changes with η.

4.3.4 Longitudinal leakage

The total thickness of the EM Calorimeter (active plus upstream material) is at least 26 X_0 over the full pseudorapidity coverage, except in the region $|\eta| < 0.4$ and in the transition between the barrel and the end-cap. This depth is sufficient to ensure that the longitudinal shower leakage does not significantly degrade the energy resolution, in particular the constant term, up to the highest energies (TeV range). Furthermore, for showers of a few hundred GeV or more, the energy resolution can be preserved by weighting the energy deposited in the back compartment of the EM Calorimeter (see Section 4.3.5).

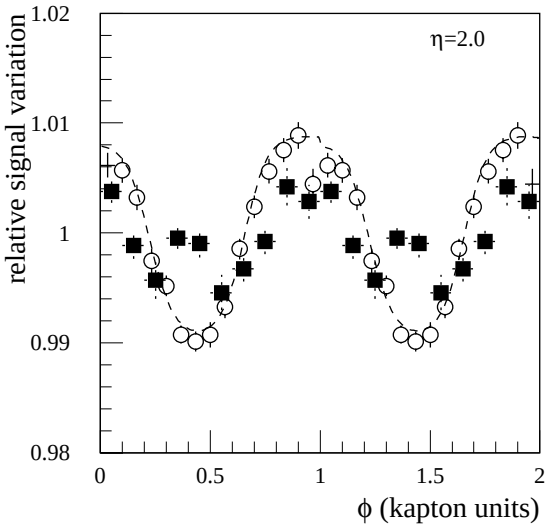

Figure 4-16 Calorimeter response to photons of E_T = 50 GeV at η = 2, normalised to the generated energy, as a function of ϕ inside one cell, when a uniform electric field (open circles) or a realistic field (solid squares) are used.

4.3.5 Energy resolution: sampling term

The results presented in this section were obtained by using the nominal cluster sizes for the different particles (electrons, unconverted photons, converted photons) described in Section 4.3.1. Furthermore, the various corrections discussed above (presampler weight, η and ϕ-modulation) were applied.

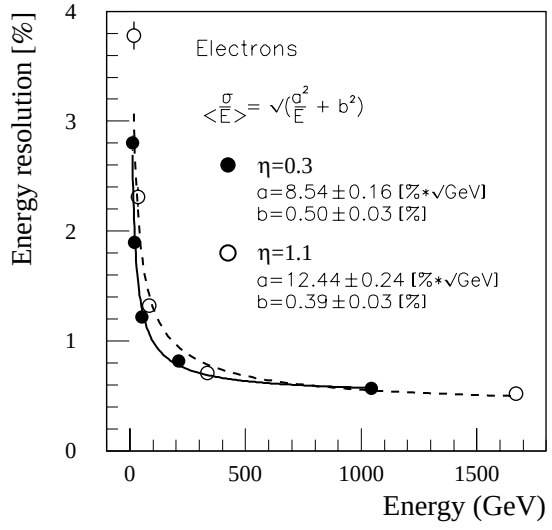

Figure 4-17 Energy resolution for electrons at η = 0.3 and η = 1.1, as a function of the incident energy.

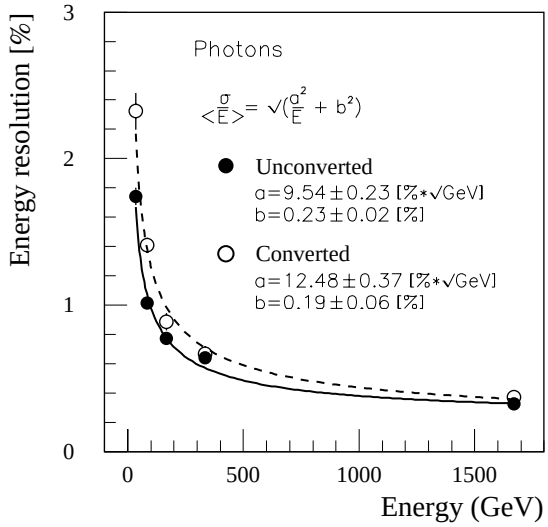

Figure 4-18 Energy resolution for converted and unconverted photons at η = 1.1, as a function of the photon energy. The fraction of converted photons is about 40% at η = 1.1.

Figures 4-17, 4-18 and 4-19 show the energy resolution, as a function of the incident energy, at various pseudorapidities. The points follow a scaling law of the type $1/\sqrt{E(GeV)}$, apart from a small local constant term (hereafter called 'cell constant term'). The latter originates mainly from residual longitudinal leakage and response modulation after correction. The sampling term is of order $10\%/\sqrt{E(GeV)}$ or smaller, except for converted photons and electrons at the end of the barrel, where the material in front of the calorimeter is large.

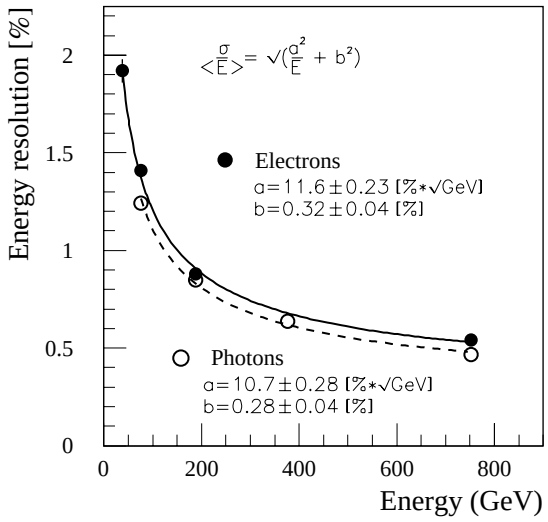

Figure 4-19 Energy resolution for electrons and photons at η = 2.0, as a function of the incident energy.

For very energetic showers, the longitudinal leakage behind the calorimeter would lead to an increase of the constant term if not compensated. By weighting the energy deposited in the back compartment (the optimum weight is ~1.3 for showers of E = 1 TeV in the barrel), an energy resolution of 0.5% or better can be achieved in the TeV range. For instance, for photons at η = 2.0, the cell constant term decreases from 0.4% to 0.28% when the energy deposited in the back compartment is weighted.

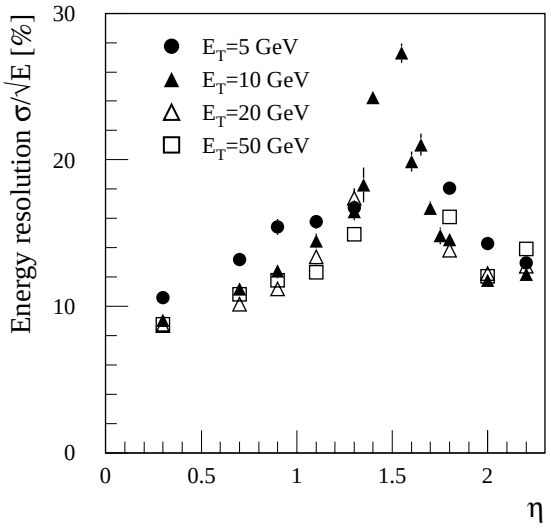

Figure 4-20 Energy resolution for electrons of various transverse energies, as a function of pseudorapidity.

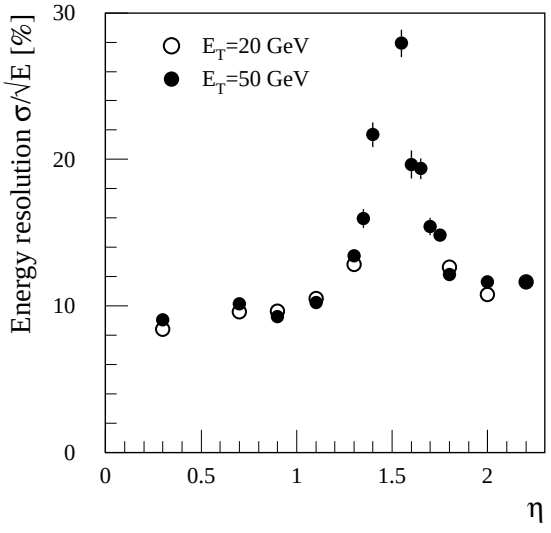

Figure 4-21 Energy resolution for photons of E_T = 20, 50 GeV as a function of pseudorapidity.

The calorimeter resolutions, as obtained over the full pseudorapidity coverage and for particles of various energies, are presented in Figures 4-20 (electrons) and 4-21 (photons). The cell constant term has not been unfolded. For this reason, these results are slightly worse than the sampling terms obtained from the fits to the points in Figures 4-17 - 4-19, especially in the end-cap region. With the exception of the crack region at $|\eta| \sim 1.5$, the dependence of the resolution on pseudorapidity follows the changes in the amount of upstream dead material and in the sampling frequency. The crack regions are discussed in more detail in Section 4.3.8.

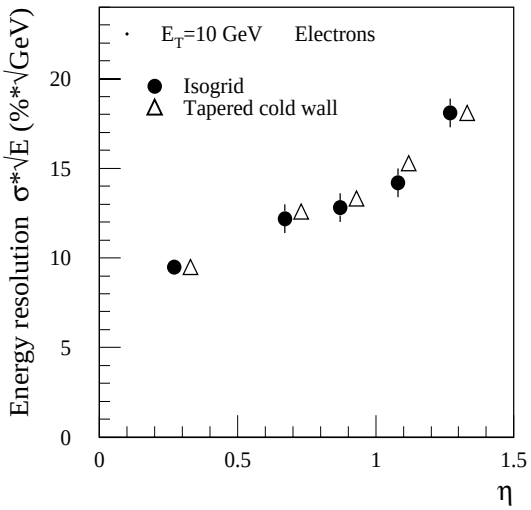

Figure 4-22 Energy resolution for electrons of E_T= 10 GeV, as function of pseudorapidity, as obtained with the old isogrid wall (dots) and the new tapered wall (open triangles) of the barrel cryostat.

One modification of the layout, which may have an impact at low energy, is the above-mentioned use of a tapered cold wall instead of an isogrid for the barrel cryostat. The sampling terms for electrons of E_T = 10 GeV, as obtained with the old isogrid wall and the new solid wall, are compared in Figure 4-22 . No significant difference is observed. This is because at small pseudorapidity, where the increase in material is largest, the total amount of material is relatively small (~2 X_0). On the other hand, at large pseudorapidity, where the amount of material is critical, the new tapered wall has an equivalent thickness similar to the isogrid wall.

Figure 4-23 shows the reconstructed energy spectra for photons of E_T = 50 GeV at η = 2.0, obtained with a realistic electric field map or with a uniform field. The calibration coefficients (Equation 4-1) determined with a uniform field have been used in both cases. The distribution obtained with a realistic field peaks at lower values, as a consequence of the lower electric field in the folds. On the other hand, there is no significant difference in the resolution and in the tails of the spectra.

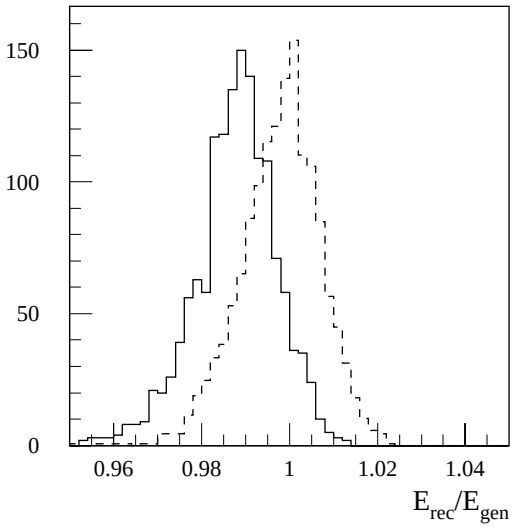

Figure 4-23 Ratio between the reconstructed and the generated energy for photons of E_T = 50 GeV at η = 2.0, as obtained when a uniform electric field (dashed line) or a realistic field (full line) are simulated. Both distributions are normalised to the same number of events.

4.3.6 Energy resolution: constant term

To meet the LHC physics requirements [4-1], the global constant term of the energy resolution, over the full calorimeter coverage relevant for precision physics, must be equal to or smaller than 0.7%. The strategy to achieve this goal is to have a small constant term, by con-

struction, over a limited region of the calorimeter coverage (the so-called 'local' constant term), and then calibrate out long-range non-uniformities *in situ* by using physics samples (*e.g.* $Z \rightarrow ee$ events).

In this section, the main sources of non-uniformities contributing to the local and overall constant term of the calorimeter resolution are discussed, and first measurements obtained with the calorimeter parts under construction are presented.

A summary of the expected contributions to the constant term is given in Table 4-3. These numbers are based on the experience gained in the construction and test of various prototypes [4-6].

4.3.6.1 The local constant term

Table 4-3 Expected short-range and long-range contributions to the overall constant term of the energy resolution.

Source	Contribution to the constant term (%)
Detector geometry (short range):	
Residual ϕ modulation, leakage, *etc.*	0.25
Variation of sampling fraction (end-cap only)	0.35
Mechanics (short range):	
Absorber and gap thickness	< 0.25
Calibration (short range):	
Amplitude accuracy and stability	0.25
Difference between calibration and physics signal	0.3
Long range:	
Signal dependence on LAr impurities	< 0.1
Signal dependence on temperature	0.2
HV variations	<0.1
Others (*e.g.* upstream material, mechanical deformations, cable lengths.)	<0.1

The goal is to achieve a local constant term over a calorimeter region of size $\Delta\eta x \Delta\phi = 0.2x0.4$, which corresponds to the size of a motherboard in the middle compartment, of 0.5%. There are 440 such regions in the whole EM Calorimeter.

In the absence of imperfections in the detector mechanics and electronics, a constant term of about 0.25% is obtained for particles incident in a given cell of the barrel (see Section 4.3.5). The main contribution to this cell constant term is the residual ϕ modulation after correction. Additional contributions to the local constant term come from mechanical and calibration non-uniformities. Adding quadratically the short-range contributions listed in Table 4-3, a local constant term of about 0.5% (0.6%) is obtained in the barrel (end-cap), which is slightly larger than the values presented in [4-1]. This is mainly due to a more conservative estimate of the last short-range contribution in Table 4-3, which comes from possible differences between the calibration and the physics signals and which is discussed in Section 4.3.6.3. Due to the limited knowledge of these effects, their sizes can only be assessed from the measurements performed with the module zero.

4.3.6.2 The overall constant term

In order to fully benefit from the good expected local constant term, it is necessary to guarantee the calorimeter long-range uniformity over the 440 regions. Several potential sources of long-range non-uniformities can be envisaged.

The liquid-argon pollution can produce non-uniform signal losses as a function of time. Although the use of fast shaping reduces the sensitivity of the response to the pollution, extensive measurements of all the materials which will be inside the cryostat have been performed, also under irradiation [4-7]. Furthermore, the calorimeter will be equipped with several probes, which will monitor the liquid-argon purity as a function of time.

The calorimeter response depends on the temperature of the liquid Argon. The signal drops by about 2% per degree, which is due to both the variation of the LAr density and the variation of the electron drift velocity. Detailed calculations of the temperature uniformity inside the barrel cryostat have started. In addition, temperature probes installed inside the cryostat will monitor the temperature variation with time [4-8], with a precision of better than 0.1 K.

The material distribution in front of the EM Calorimeter, possible small deformations of the calorimeter, the different lengths of the calibration cables, chosen to compensate for the particle time of flight in physics events, could give rise to additional response non-uniformities. However, these non-uniformities do not vary with time, and therefore corrections should be more straightforward.

In addition to the monitoring system based on probes, the long-range non-uniformities can be monitored and corrected *in situ* by using control physics samples such as $Z \rightarrow ee$ events. This is discussed in Section 4.6.2.

4.3.6.3 Detector uniformity measurements

Parts of the EM Calorimeter have already been built and prototypes of the electronics, operational in test beams, exist. Preliminary measurements have been performed in order to check whether the requirements for the constant term are satisfied. A selection of these measurements is discussed below.

Lead thickness. The lead plates for the whole EM Calorimeter have been delivered. The thicknesses have been measured with two methods: a fast on-line method during the rolling process based on X-ray absorption, and a more careful off-line method based on ultrasound [4-9]. The distribution of the average plate thickness, as obtained from the on-line measurements, is shown in Figure 4-24 for the full set of 2048 plates equipping the barrel region $|\eta| > 0.8$ (nominal Pb thickness is 1.13 mm). If the plates were assembled randomly, the dispersion (~7 μm) would already

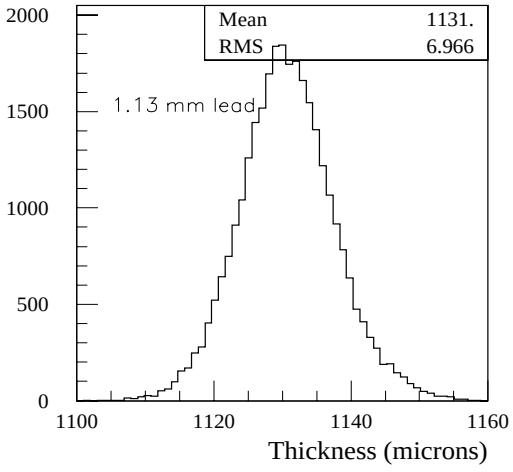

Figure 4-24 Distribution of the thickness of the 2048 lead plates for the half-barrel region $|\eta| > 0.8$, as measured at several positions inside the plates.

result in a contribution to the constant term of less than 0.2%, which is within the requirements mentioned above. In order to further minimise the response variation due non-uniformities in the absorber thickness, an algorithm has been developed to sort and pair the absorber plates [4-10]. It minimises the thickness dispersion computed over five plates, by considering several combinations of plates. The contribution of the fluctuations in the plate thicknesses to the constant term is about 0.6 x $\sigma^{(5)} / e_n$, where $\sigma^{(5)}$ is the rms of the mean thickness of the five plates and e_n the nominal thickness of the plates. Table 4-4 shows the improvement due the pairing procedure for the absorbers of the barrel module zero. For the 1.13 mm plates the dispersion decreases by almost a factor of two, whereas no improvement is observed for the 1.53 mm plates since the original distribution is already very good.

Table 4-4 For the plates of the barrel module zero, the overall dispersion in the thicknesses, and the normalised dispersion over five absorber plates as obtained without and with pairing.

Lead plates thickness	Rms dispersion	$\sigma^{(5)}/e_n$ without pairing	$\sigma^{(5)}/e_n$ with pairing
1.13 mm	8.5 μm	7.4×10^{-3}	4.1×10^{-3}
1.53 mm	6.8 μm	2.3×10^{-3}	2.2×10^{-3}

Calibration system. To correct the gain dispersion of the electronic channels, which is of order a few percent, a precise calibration system is required.

A calibration pulse which simulates the triangular signal from the calorimeter, with a fast rise-time and a very precise amplitude, is required. Calibration boards, with 128 channels, have been designed and built for the beam tests. The measurements demonstrate good linearity over a 16-bit dynamic range and good uniformity. Figure 4-25 shows the pulse amplitude, as a function of the channel number, for a few boards already characterised. The dispersion of 0.11% is compatible with the intrinsic limitation of the injection resistors [4-2].

The signal is sent through cables to the motherboards and then distributed to the calorimeter. Since the calibration cables are terminated at both ends, the amplitude is not very sensitive to the characteristic impedance of the cables. However, production tolerances on the impedance dispersion from cable to cable at the level of 4% rms are needed to achieve the required uniformity of the calibration system. Such precision has been obtained for the cables built for the module zero's [4-11]. The uniformity of the calibration signal has been measured including cables and pin carrier, in order to simulate the ATLAS set-up, and no sizeable deterioration of the amplitude dispersion has been observed.

Physics and calibration signals do not follow exactly the same path, which can give rise to differences between them. In particular, any inductance in parallel with the calibration signal but in series with the physics signal introduces amplitude differences. Such inductances exist by construction in the electrodes and have to be corrected for. Moreover, cross-talk affecting differently the physics and the calibration signals would also introduce non-uniformities. A careful design of the motherboards is being developed, in order to minimise additional sources and to ensure small cross-talk. Measurements of these effects with module zero's are foreseen in the near future.

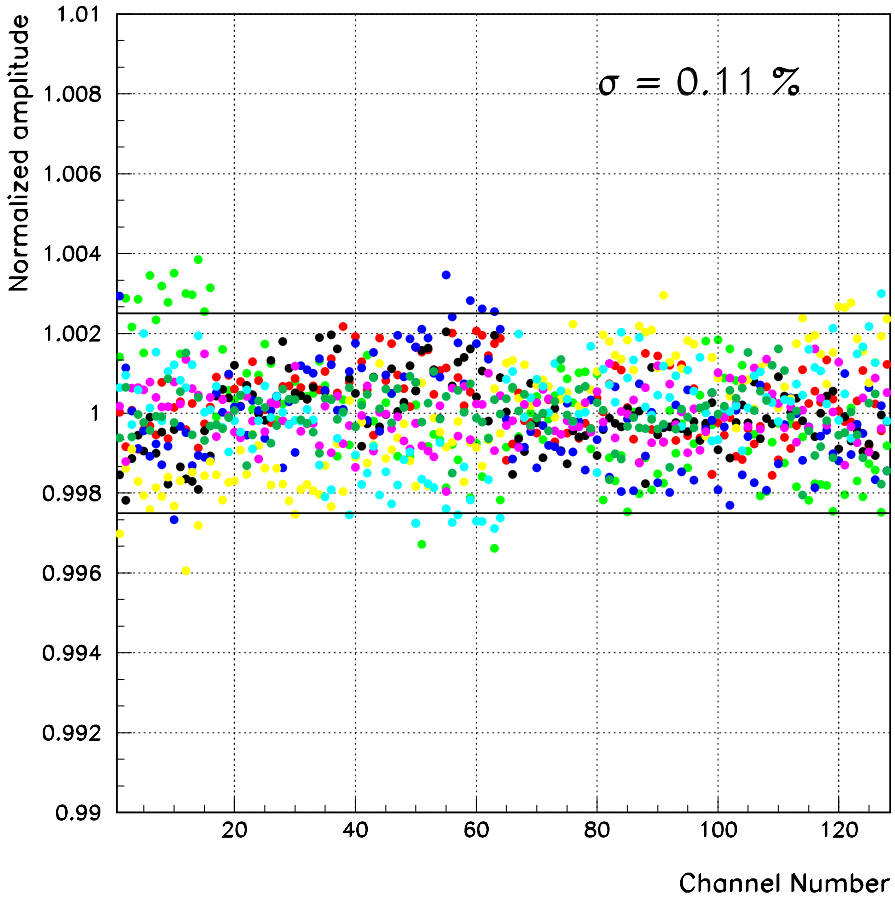

Figure 4-25 Normalised output signals from eight calibration boards, as a function of the channel number.

4.3.7 Low-energy tails

Most of the low-energy tails in the energy spectra reconstructed in the EM Calorimeter are caused by the material in the Inner Detector. A photon / electron shower which starts in the Inner Detector is opened in ϕ by the magnetic field, the effect being larger for smaller particle energies and interaction radii. As a consequence, the shower energy is not completely contained in the calorimeter cluster, and low-energy tails appear in the calorimeter energy distributions. For this reason, asymmetric clusters (larger in ϕ than in η) are used, which are bigger for electrons (3x7 cells) than for photons (3x5 cells).

The material distribution in the Inner Detector is shown in Figure 3-5, and the evolution since the detector TDR's is discussed in Section 3.2.1.

The dependence of the low-energy tails on the particle interaction radius is illustrated in Figure 4-26, which shows the distribution of the radius at which the electron has radiated the hardest bremsstrahlung photon, for electrons of E_T = 10 GeV at η = 1.2. At this pseudorapidity, the material in the Inner Detector reaches 0.8 X_0. Clear peaks are visible at the positions of the Pixel and Silicon layers (at this pseudorapidity the electron track crosses only three SCT layers before entering the end-cap region), as well as a continuous distribution in the TRT region. The open histogram is for all electrons and the shape and height of the peaks simply reflect the dis-

tribution and amount of material in the various parts of the Inner Detector. The black histogram is for electrons in the low-energy tails of the calorimeter energy measurement, *i.e.* electrons for which the reconstructed energy is smaller than 92% of the true energy. At this pseudorapidity, the fraction of events in the tails is $(19.2 \pm 0.6)\%$. It can be seen that the tails are populated mainly by electrons which have interacted in the internal layers of the Inner Detector. A more quantitative estimate of the contribution of the various parts of the Inner Detector to the tails is given in Table 4-5. Each of the pixel and SCT layers produces about 2% of the tail. A similar contribution comes from the ensemble of the TRT and the services running at the outer radius, despite the fact that the total material in this region is much larger than in a single precision layer. Some decrease of the tail with radius is visible also in the three SCT layers.

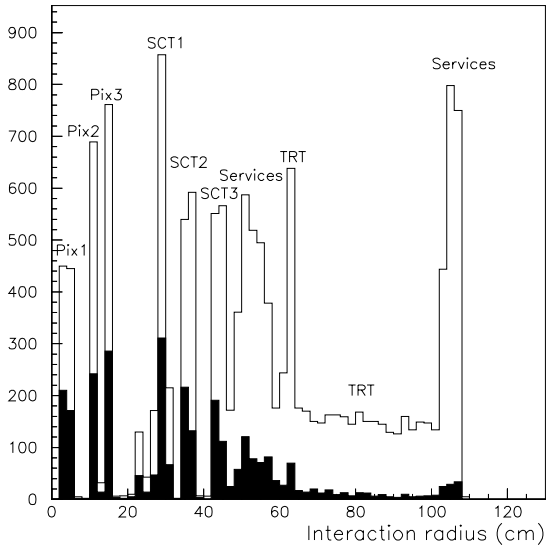

Figure 4-26 Distribution of the radius at which the electron has emitted the hardest Bremsstrahlung photon for electrons of E_T = 10 GeV at η = 1.2. The white histogram is for all electrons, the black histogram is for electrons in the low-energy tail of the calorimeter spectrum.

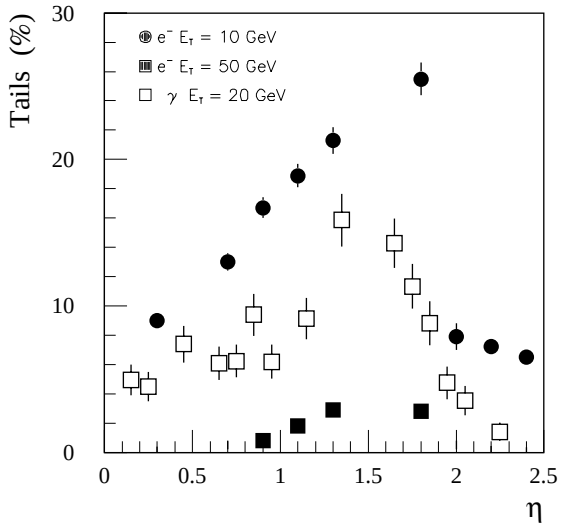

Figure 4-27 Fraction of events for which the energy reconstructed in the EM Calorimeter is smaller than 92% of the true energy, as a function of pseudorapidity and for electrons and photons of various transverse energies.

Figure 4-27 shows the tails for electrons and photons of various transverse energies, as a function of pseudorapidity. The distribution of the points in Figure 4-27 reflects mainly the material profile in the Inner Detector shown in Figure 3-5. By combining the information of the Inner Detector and of the calorimeter, it is possible to reduce the tails by 20%. This is discussed in Chapter 7.

4.3.8 Crack regions

There are regions in the EM Calorimeter acceptance where the detector performance is degraded. These regions, which correspond to the transitions in η between mechanically independent detector modules, are:

- A 6 mm wide liquid-argon gap between the two half barrels at $\eta = 0$. As already mentioned in Section 4.1.1, since the time of the Calorimeter TDR the cold flange, which was

Table 4-5 Contributions to the calorimeter low-energy tails coming from the various layers of the Inner Detector. The errors are ~0.2%.

	Contributions to tails (%)
Beam pipe	0.5
Pixel barrel 1	2.2
Pixel barrel 2	2.3
Pixel barrel 3	2.2
Pixel support	0.4
SCT barrel 1	2.5
SCT barrel 2	2.2
SCT barrel 3	1.9
SCT services	2.4
TRT	2.4
TOTAL	19.2 ± 0.6

located at $\eta \sim 0$, has been moved to the end of the barrel, thus reducing the amount of material in this region. As a consequence, the detector response is degraded over a region of size $|\Delta\eta| < 0.01$, which is narrower than in [4-1]. No further discussion of this region is presented here.

- A 3 mm wide liquid-argon gap at $|\eta| \sim 2.5$ between the outer and the inner wheel of the end-cap calorimeter, which is preceded by the end-cap intermediate support ring. Since the detector response is deteriorated over a very small region of size $|\Delta\eta| < 0.01$, and since nothing has changed with respect to the results reported in [4-1], no further discussion of this region is presented here.
- The transition between the barrel and the end-cap calorimeters at $|\eta| \sim 1.5$. Since a few changes have been made to the layout of this region after the Calorimeter TDR, and since this transition gives rise to the largest crack in the calorimeter acceptance, an update of the detector response around $|\eta| \sim 1.5$ is presented below (Section 4.3.8.1).
- Gaps between presampler sectors. A detailed study has been performed of the energy losses in the small inactive gaps between the barrel presampler modules [4-12]. The results are presented in Section 4.3.8.2.

The absence of cracks in azimuth is an intrinsic feature of the accordion geometry.

4.3.8.1 Barrel/end-cap transition region

A detailed description of the detector response in this region is given in [4-1], therefore only an update is presented here.

The layout of the transition between the barrel and the end-cap calorimeter is shown in Figure 4-i and the material in front of it in Figure 4-iii. The barrel and end-cap calorimeters are housed in two different cryostats, separated by 9.5 cm of space used to route services and cables of the Inner Detector. Particles incident at $|\eta| \sim 1.5$, that is at the end of the barrel calorimeter,

where the dead material in front of the end-cap calorimeter reaches a maximum of 7 X_0, cross six cryostat walls, the edge of the coil, cables and services and several layers of dead liquid before reaching the end-cap calorimeter. For larger pseudorapidities, the material is smaller because the coil and the cold wall of the barrel cryostat do not contribute.

Since the time of Calorimeter TDR, the amount of material in this region has slightly increased (see Figure 4-9). The new tapered wall has a marginal impact on the material at the end of the barrel, whereas the cold flange of the barrel cryostat adds about 1.5 X_0 at $\eta \sim -1.5$ and the Inner Detector services add 0.4 X_0 at the end of the barrel, with respect to the layout in [4-1]. It is stressed again that the increase by about 0.8 X_0 at $|\eta| \sim 1.7$ in Figure 4-9 is due to the fact that in the detector simulation used for the studies presented here the warm flange had titanium (instead of aluminium) bolts. Therefore these results are somewhat conservative.

Energy losses in this region can be, to a large extent, recovered by using two dedicated devices: the end-cap presampler, which covers the region $1.5 < |\eta| < 1.8$, and a scintillator slab, which covers the region $1.0 < |\eta| < 1.6$.

The energy response at the barrel/end-cap transition is shown in Figure 4-28 for low-energy electrons, which are most sensitive to the dead material. The uncorrected response drops by more than a factor of two at the end of the barrel calorimeter. By using the energy deposited in the presampler and in the scintillator, suitably weighted, the average response can be recovered.

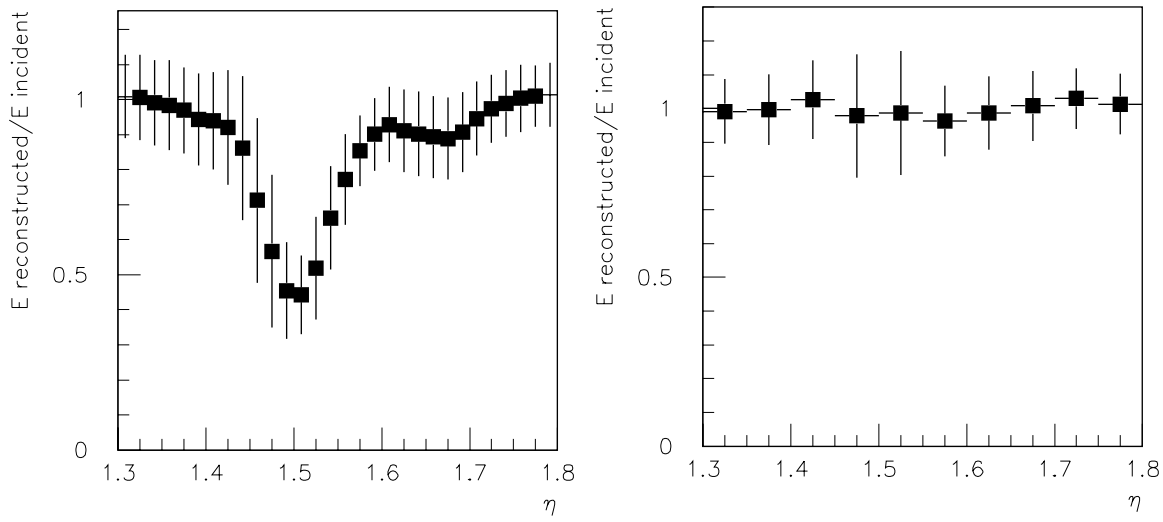

Figure 4-28 Ratio between the energy reconstructed in the calorimeter (3x7 cell cluster) and the incident energy, as a function of pseudorapidity in the barrel/end-cap transition region, for electrons of E_T = 10 GeV, before (left) and after (right) adding the (weighted) energy in the presampler and in the scintillator. The error bars give the rms spread on the reconstructed energy.

The correlation between the energy deposited in the presampler and in the calorimeter, which is exploited to compensate for the energy lost upstream of the calorimeter, is depicted in Figure 4-29. Figure 4-30 shows the energy resolution in the transition region for electrons of E_T = 10 GeV and photons of E_T = 50 GeV. It can be seen that adding the presampler and the scintillator weighted energies improves the energy resolution by up to a factor of three. The resolution at $|\eta| \sim 1.5$ is a factor of two worse than in [4-1], as a consequence of the larger material in the transition region with the present layout. For precision physics, fiducial cuts are applied in this region over a rapidity range of size $|\Delta\eta| \sim 0.15$.

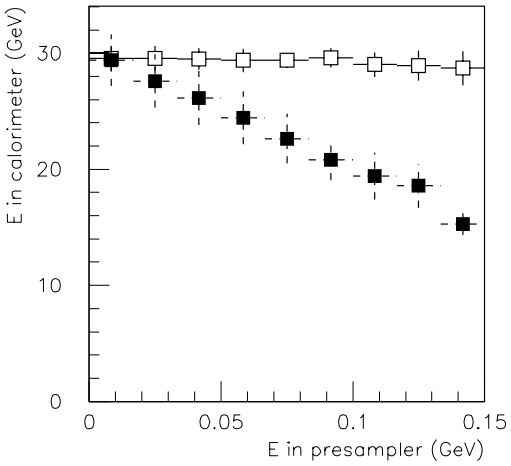

Figure 4-29 Calibrated energy reconstructed in the calorimeter, as a function of the energy deposited in the presampler, for electrons of E = 30 GeV at $\eta \sim 1.7$, before (closed symbols) and after (open symbols) adding the (weighted) presampler energy.

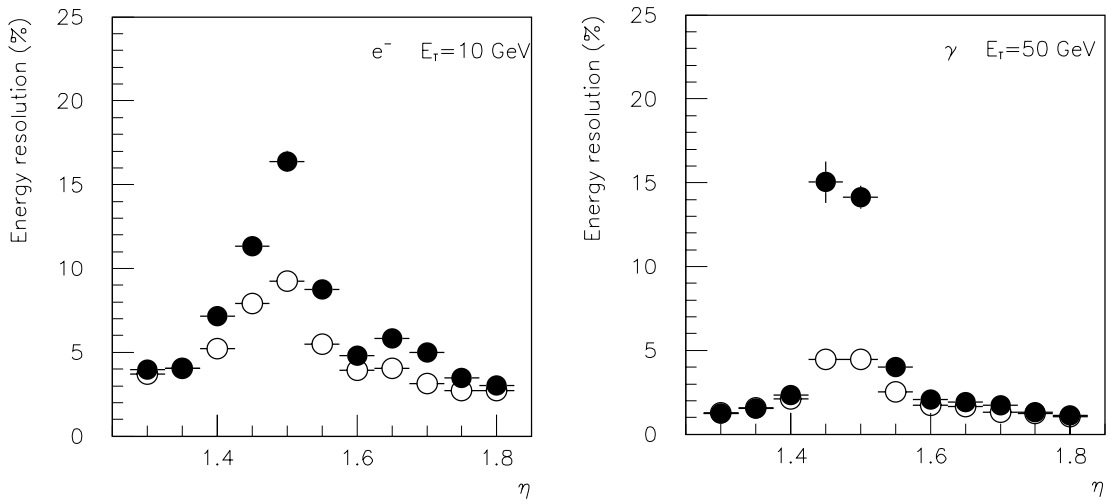

Figure 4-30 Energy resolutions for electrons of E_T = 10 GeV (left) and photons of E_T = 50 GeV (right), as a function of pseudorapidity in the transition region, before (closed symbols) and after (open symbols) adding the weighted energy deposited in the presampler and in the scintillator. Electronic and pile-up noise are not included. A 3x7 cell cluster has been used.

4.3.8.2 Gaps between presampler sectors

There is a gap between the barrel presampler sectors in the ϕ direction. At the temperature of liquid argon, this gap is about 1.8 mm wide: the clearance between the skirts is around 1 mm while the skirt thickness is 0.4 mm. Furthermore, the distance between the skirt inner conductive surface and the copper edge of the anode is 2 mm. The fraction of energy ρ which is not measured because of these gaps was determined by using a two-dimensional map of the electric field and full charge collection. The probability that a fraction ρ of the presampler energy is lost because of the gaps is shown in Figure 4-31. For electrons of E_T = 10 GeV at η = 0.9, on average 1.3% of the energy deposited in the presampler is lost in the gaps, which corresponds to 0.1% of the total shower energy. The influence of the presampler gaps on the energy measured in the presampler and in the calorimeter is therefore small.

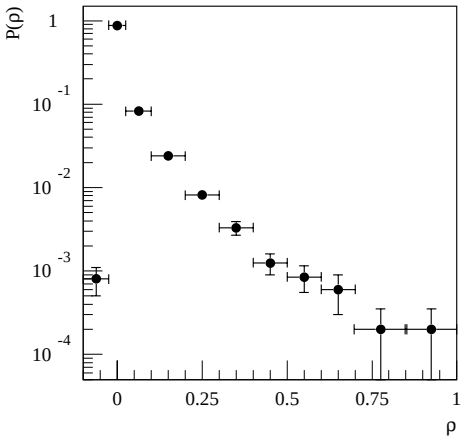

Figure 4-31 Probability that a fraction ρ of the presampler energy is lost due to the gaps between sectors for electrons of E_T = 10 GeV at η = 0.9.

4.3.9 Total energy resolution

The total energy resolution of the calorimeter includes the contributions of the sampling term, of the constant term (0.7%) and of the electronic and pile-up noise expected at low or high luminosity, individually discussed in the previous sections.

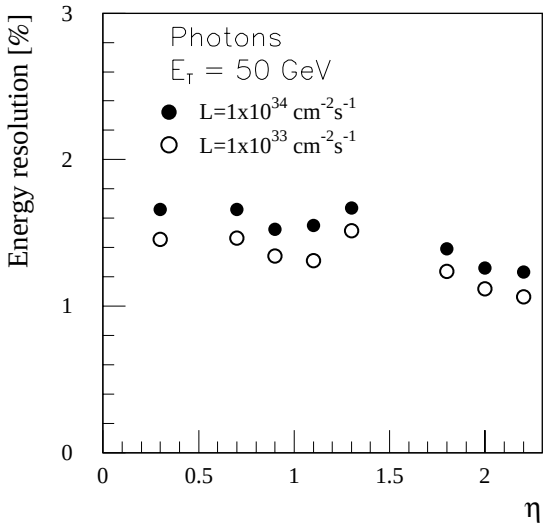

Figure 4-32 Total energy resolution for photons of E_T = 50 GeV, as a function of pseudorapidity, as obtained at low (open symbols) and high (closed symbols) luminosity.

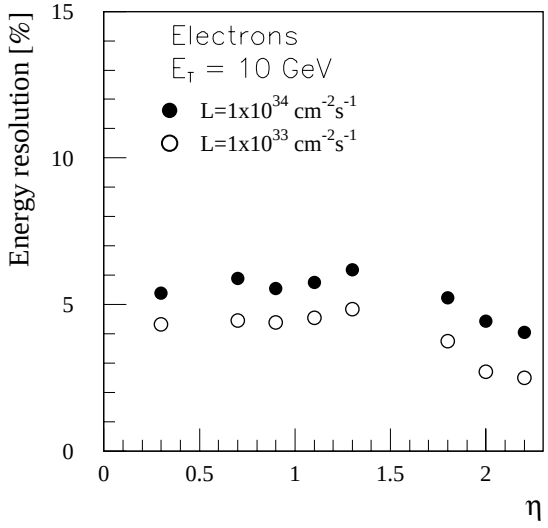

Figure 4-33 Total energy resolution for electrons of E_T = 10 GeV, as a function of pseudorapidity, as obtained at low (open symbols) and high (closed symbols) luminosity.

For photons of moderate E_T (Figure 4-32) the total resolution is of order 1.6% or better at all luminosities over most of the pseudorapidity coverage. For low-energy electrons (Figure 4-33) the total resolution is about 5% (3%) in the barrel (end-cap). This performance ensures mass resolutions of order 1.5 GeV for $H \to \gamma\gamma$ and $H \to eeee$ decays with $m_H \sim 100$ GeV (Chapter 7), and therefore good sensitivity to both these channels (see Chapter 19).

The impact of the electronic noise and pile-up on the reconstructed energy spectra for low-energy electrons is further illustrated in Figure 4-34. Distributions are shown for the case of no noise and no pile-up, for the noise and pile-up expected at low luminosity, and for the noise and pile-up expected at high luminosity. The smearing of the energy spectrum with increasing noise is evident.

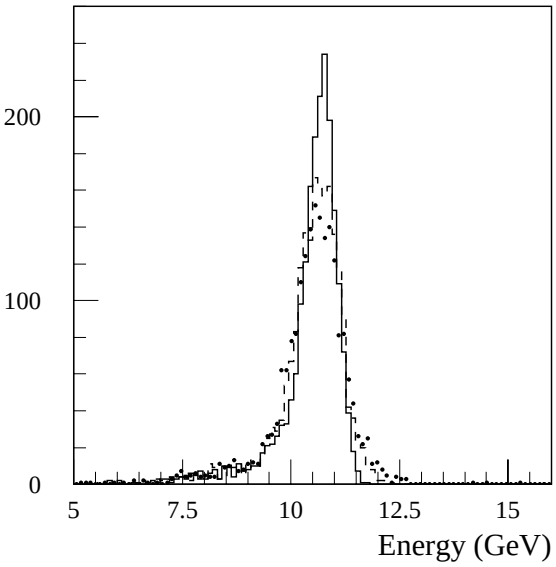

Figure 4-34 Energy spectra for electrons of E_T = 10 GeV at η = 0.3, as obtained without pile-up and noise (full line) and with the pile-up and noise expected at low luminosity (dashed line) and high luminosity (dotted line). The three distributions are normalised to the same number of events.

4.4 Position and angular measurements

The excellent longitudinal and lateral granularity of the EM Calorimeter, in particular of the strip section, allow several measurements of the shower position to be performed with high precision. The position in ϕ can be measured in the middle compartment and the position in η can be measured in the strip section and in the middle compartment. By combining the measurements of the shower η–position obtained in the first two compartments, it is possible to determine the shower direction in θ, and therefore to measure the position of the primary vertex along the z axis ('pointing'). Indeed, the z-position of the primary vertex is not known unambiguously at high luminosity in events with a $H \to \gamma\gamma$ decay, and therefore the angular information from the calorimeter is needed to obtain a precise reconstruction of the Higgs mass. By using the same method it is also possible to tag photons which do not come from the primary vertex. Such photons are predicted by Gauge-Mediated-Supersymmetry-Breaking theories (see Chapter 20).

The various position and angular measurements provided by the EM Calorimeter are discussed below.

4.4.1 Measurement of the position in ϕ

The ϕ position of a cluster is measured in the middle compartment. Because of the accordion shape of the cells, the measured position is affected by an offset, which depends on the shower depth and which is corrected for as described in [4-1]. Figure 4-35 shows the ϕ-resolution obtained for unconverted photons of E_T = 20 and E_T = 50 GeV without pile-up and electronic

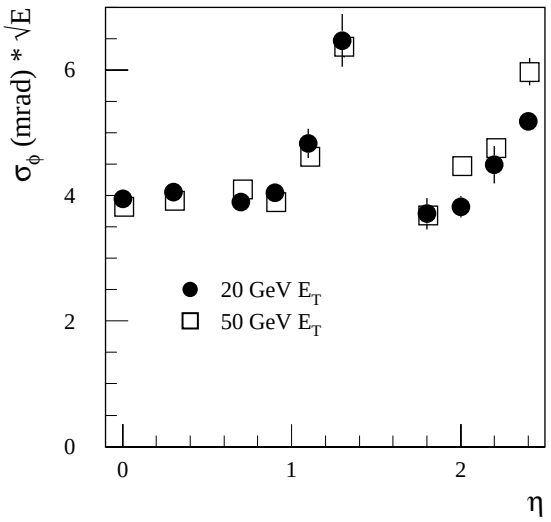

Figure 4-35 Calorimeter resolution in ϕ, as a function of pseudorapidity, for unconverted photons of E_T = 20 GeV and E_T = 50 GeV.

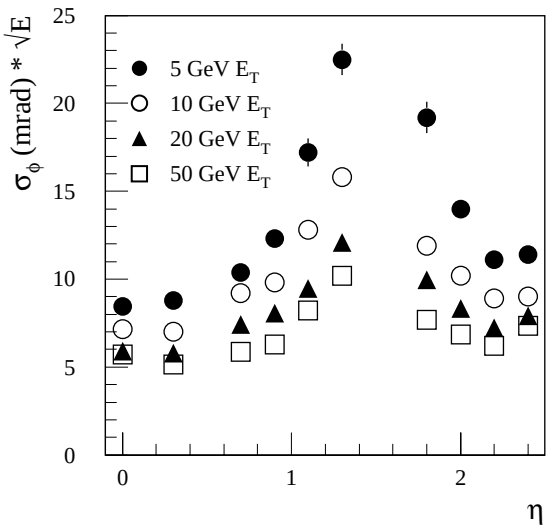

Figure 4-36 Calorimeter resolution in ϕ, as a function of pseudorapidity, for electrons of various transverse energies.

noise. The calorimeter resolution scales as 4-6 mrad / $\sqrt{E}$, corresponding to 6.5-10.5 mm / $\sqrt{E}$ in the barrel and to 4-5 mm / $\sqrt{E}$ in the end-caps. The scaling law $1/\sqrt{E}$ is not valid for electrons, which emit bremsstrahlung in the Inner Detector. Figure 4-36 shows that the ϕ-resolution for electrons degrades faster at low energies.

Electronic noise and pile-up at high luminosity deteriorate the position resolution for E_T = 5 GeV electrons by up to a factor of two if the standard cluster of 3x7 cell is used. A smaller window (3x5 cells) is therefore more suitable to measure the shower position for low-energy particles at high luminosity.

The use of the calorimeter ϕ-position measurement for many physics applications is illustrated in Chapter 7.

4.4.2 Measurement of the position and direction in η

4.4.2.1 Photons coming from the vertex

In order to reconstruct the $H \rightarrow \gamma\gamma$ invariant mass at high luminosity, the calorimeter must be able to measure the direction of both photons in η with high precision. This measurement makes use of the reconstructed shower positions and shower depths in the strip and middle compartments. Corrections for the modulation of the reconstructed position with the particle impact point ('S-shapes') have to be made to achieve a good resolution.

The shower depths in the calorimeter and the S-shape corrections in the first compartment were determined in the same way as in [4-1]. As the dominant contribution to the final resolution in the photon direction comes from the S-shape corrections in the middle compartment, an attempt has been made to improve these corrections.

The S-shapes depend on:

- The position $\eta^* = \mathrm{mod}(\eta, 0.025)$ of the shower in the cell, relative to the cell boundaries.
- The shower depth, which depends on the material in front of the calorimeter and on the particle energy. This depth fluctuates event by event and is strongly correlated with the fraction of energy *F1* measured in the first compartment.
- The shower pseudorapidity, especially in the end-caps, because the physical cell size decreases with respect to the shower size as η increases.

Two feed-forward multilayer neural networks (NN) have been used to fit the S-shape corrections as a function of (η^*, η, F_1) in the barrel and in the end-caps. More details about this method are given in [4-13].

The resolutions of the measurements of the shower η–positions in the first two compartments of the calorimeter are presented in Figure 4-37. From these two measurements one can obtain the photon direction in θ, after dividing by the lever arm, and thus a measurement of the position of the primary vertex in *z*. The calorimeter angular resolution obtained in this way is shown in Figure 4-38. It is of the order of 60 mrad / $\sqrt{E}$, where *E* is measured in GeV. The resulting resolution on the reconstructed *z*-position of the vertex is shown in Figure 4-39. The use of a better correction in the middle compartment improved the *z*-resolution by 10% to 20% at all pseudorapidities with respect to the results presented in [4-1]. If the electronic and pile-up noise expected at high luminosity are included, the vertex resolution degrades by about 20%.

In $H \rightarrow \gamma\gamma$ events, two photons are available in the final state, and the primary vertex can be reconstructed as the weighted average of the two vertices provided by both photons plus the constraint that the nominal vertex position is at $z = 0$ and has a dispersion of $\sigma = 5.6$ cm. The vertex obtained in this way is compared to the true vertex in Figure 4-40. The precision of the vertex measurement provided by the calorimeter alone, averaged over the full pseudorapidity coverage, is 1.3 cm. Tails are small, given that about 87% of the events are contained within $\pm 2\sigma$, where $\sigma = 1.3$ cm, from the peak of the distribution.

It is expected that the readout electrodes of the EM Calorimeter will be mutually aligned in z with a dispersion of about ±400 μm. The impact of this non-perfect alignment on the position and angular measurements has been evaluated, and the results have been used to define the mechanical tolerances. In the simulation each of the 1024 electrodes was displaced by an amount randomly chosen in the range ±400 μm or ±1000 μm around the nominal position. The shower position was reconstructed using corrections determined with perfect alignment. The results are summarised in Table 4-6.

Table 4-6 Resolution in the position, angle and vertex measurements, as obtained from the calorimeter for photons of E_T = 50 GeV at η = 0.3 and for three dispersions in the electrode alignment.

Dispersion	**0 μm**	**±400 μm**	**±1000 μm**
σ_η strip section	$(0.217 \pm 0.005)\times10^{-3}$	$(0.215 \pm 0.008)\times10^{-3}$	$(0.274 \pm 0.009)\times10^{-3}$
σ_η middle compartment	$(0.695 \pm 0.013)\times10^{-3}$	$(0.652 \pm 0.021)\times10^{-3}$	$(0.657 \pm 0.021)\times10^{-3}$
σ_θ (mrad)	8.270 ± 0.180	7.180 ± 0.260	7.540 ± 0.250
σ_z (cm)	1.380 ± 0.030	1.268 ± 0.043	1.260 ± 0.042

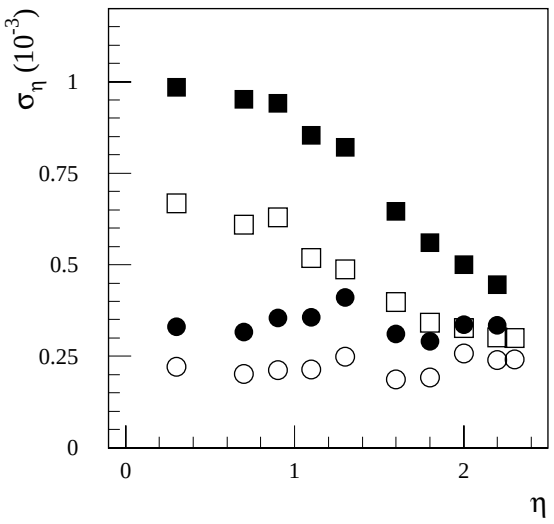

Figure 4-37 Position resolution in the η–direction, as measured in the strips (dots) and in the middle compartment (squares), as a function of pseudorapidity, for photons of E_T = 20 GeV (closed symbols) and E_T = 50 GeV (open symbols).

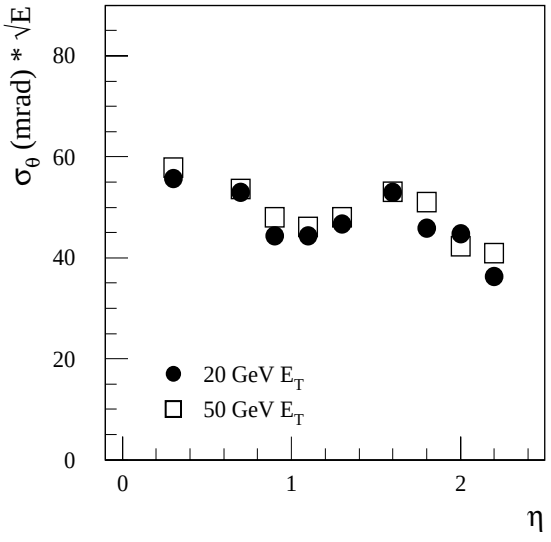

Figure 4-38 Calorimeter angular resolution in θ, as a function of pseudorapidity, for photons of E_T = 20 GeV and E_T = 50 GeV.

The position resolution in the strip section degrades with the increasing dispersion, as expected since the considered dispersions are comparable to, or larger than, the intrinsic resolution of the strips. On the other hand, the angular and vertex resolutions are not affected by the misalignment, at least up to ±1000 μm, because when the electrode position is displaced, both compartments are displaced in the same direction and by the same amount.

4.4.2.2 Non-pointing photons

As discussed in more detail in Chapter 20, Gauge-Mediated-Supersymmetry-Breaking (GMSB) models can give rise to a long-lived lightest neutralino (χ_1^0), which could decay via $\chi_1^0 \rightarrow \tilde{G}\gamma$ inside the volume of the Inner Detector. With typical χ_1^0 masses of order 100 GeV, the decay into a massless photon and a very light Gravitino (mass ≈ keV) often produces a finite opening angle. Since both the χ_1^0 and the Gravitino escape detection, the photon would provide the only evidence of the decay, and the signature would be that of an isolated photon which does not point back to the main event vertex.

As described previously, the segmentation of the EM Calorimeter has been designed to allow measurement of photon direction by using the lateral and the longitudinal positions of the shower in the strip section and in the middle compartment. While the geometry of the EM Calorimeter has been optimised for the case of photons which point back to the interaction point, the fine segmentation allows reasonable angular precision to be achieved over a wide range of photon impact angles.

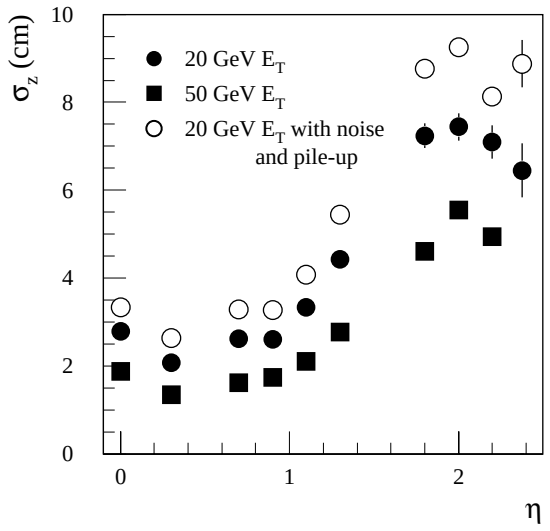

Figure 4-39 Resolution in the position of the primary vertex along the z axis, as obtained from the calorimeter pointing with single photons of E_T = 20 GeV (with and without pile-up and noise) and E_T = 50 GeV.

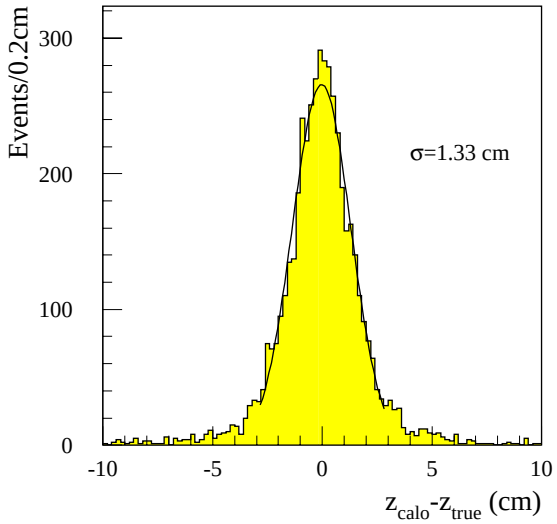

Figure 4-40 The difference between the reconstructed vertex, provided by the EM Calorimeter alone, and the generated vertex, as obtained for $H \rightarrow \gamma\gamma$ events with m_H = 100 GeV.

To study quantitatively the angular resolution for 'non-pointing' photons, two different samples of single photons were used. The first sample consisted of 20000 single photons, as produced from χ_1^0 decays in GMSB events with the GMSB parameters set to the values discussed in Section 20.3.2.4. Of these, over 7500 photons were fully simulated in the detector. In addition, the full sample of 20000 events was studied using parametrisations of the resolution function. The mean E_T of these photons, for which several distributions are presented in Section 20.3.2.4, is 84.4 GeV. The GMSB simulation shows that over 75% of the photons of interest impact the EM barrel calorimeter. For this reason, only photons hitting the barrel were considered. The second sample comprised several sets of fully-simulated 50 GeV photons, impacting the calorimeter at a given value of pseudorapidity and from a given direction. The sets were generated at pseudorapidity values of 0.3, 0.7 and 1.2, and with angular deviations from pointing of 0°, ±15°, and ±30° in θ, as well as 0°, 7° and 19° in azimuthal angle. The electronic noise was not included in the analysis discussed here, but should have a small impact on the results because of the large photon energies.

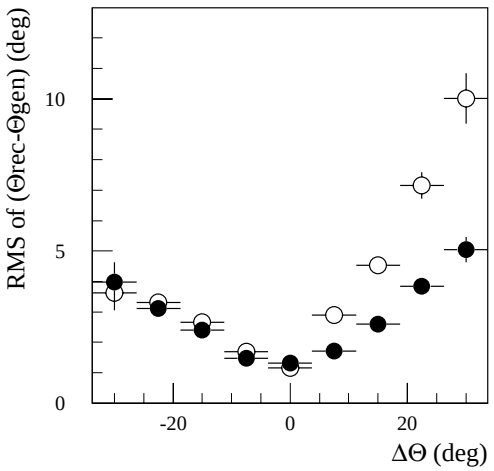

Figure 4-41 Angular resolution as a function of Δθ, the deviation from pointing, for GMSB photons with $0 < \eta < 1.4$, as obtained with the standard reconstruction (open symbols) and with a neural network (closed symbols).

For both samples of photons, the reconstruction of the photon direction was studied as a function of the impact point and the angular deviation from pointing. Although the ϕ measurement would slightly increase the ability to separate pointing from non-pointing photons, only the θ

measurement was used in the study presented here.The angular resolution obtained with the standard reconstruction algorithm (using a 7x7 cell cluster) is shown, as a function of the angular deviation from pointing ($\Delta\theta$), in Figure 4-41 for the GMSB photon sample and in Figure 4-43 for the sample of 50 GeV photons with fixed η, $\Delta\theta$ and $\Delta\phi$. Here $\Delta\theta$ and $\Delta\phi$ indicate the difference between the direction of the photon trajectory inθ and ϕ and the direction which goes from the vertex to the calorimeter impact point. The resolution from the standard reconstruction is seen to degrade significantly for large absolute values of $\Delta\theta$ and differently for different signs of $\Delta\theta$. This is due to the fact that the S-shape corrections used (see Section 4.4.2.1) are tuned for pointing events. For large deviations from pointing, these corrections are no longer valid and actually deteriorate the angular resolution. Also, for severely non-pointing showers, the cluster window considered by the standard reconstruction (which assumes pointing) is no longer centred properly on the actual cluster, and starts to lose energy leaking outside the cluster. Finally, the mean longitudinal positions of the shower in the first and second compartments have been determined by using the barycentres obtained for pointing showers, and again, for large deviations from pointing, these values are no longer valid. This effect gives rise to systematic shifts of the mean value θ reconstructed for non-pointing showers (Figure 4-42).

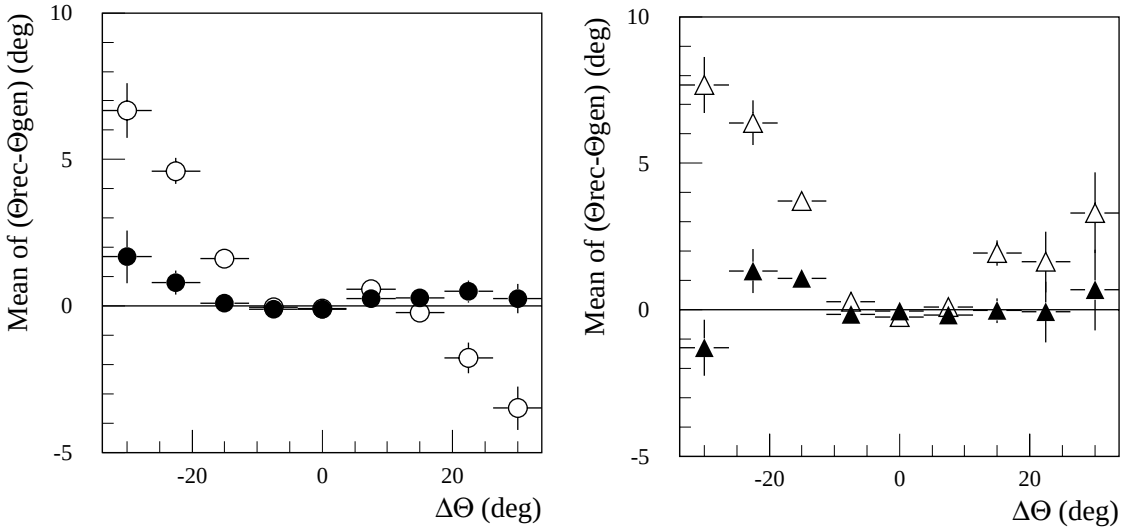

Figure 4-42 Mean of the deviation of the reconstructed value of θ from the generated value, as a function of $\Delta\theta$, for GMSB photons with $0 < \eta < 0.6$ (left) and $0.6 < \eta < 1.2$ (right), as obtained with the standard reconstruction (open symbols) and with a neural network (closed symbols).

Given this non-optimal performance of the standard reconstruction, two different algorithms have been investigated to take better into account the feature of non-pointing showers. These approaches and their performance are discussed briefly below. Details can be found in [4-14].

One approach uses a feed-forward multilayer neural network (NN) with three layers of nodes. The NN inputs were the uncorrected shower positions in the first and middle compartment, the position $\eta^* = \mathrm{mod}(\eta, 0.025)$ of the shower in the cell for the first and middle compartment, the total reconstructed energy of the shower, the energy deposited in the strip section compared to the sum of the energies in the strip section and in the middle compartment ($E_1/(E_1+E_2)$), and the value of θ from the standard reconstruction. The generated θ for each event was used as the target to train the NN on half of the GMSB photon sample. The results were then tested on the second half of the sample. The NN resolution is shown in Figure 4-41 and the mean value of the difference between the reconstructed and generated values of θ is shown in Figure 4-42. The

NN improves the resolution and also gives a smaller systematic shift compared to the standard reconstruction. The same NN reconstruction was applied to the sample of photons generated at constant values of $\Delta\theta$ and $\Delta\phi$. It was seen that the θ reconstruction was not significantly affected by deviations from pointing in ϕ. Therefore, the results for the θ resolution can be applied independently of deviations in ϕ.

The NN was trained on a sample of photons with a wide range of deviations from pointing. Not surprisingly, the resolution for pointing photons as obtained with the NN is inferior to that of the standard reconstruction, which has been tuned to the case of pointing photons.

A second algorithm, called 'the nearest neighbour clustering', does not restrict itself to a specific cluster size. The algorithm begins with the highest energy cell in the middle compartment of the EM Calorimeter and compares the energy deposited in the adjacent cells to that in the most energetic cell. If the fractional energy deposited in an adjacent cell exceeds a preset threshold (1.5% of the most energetic cell), the cell is accepted as a part of the cluster. This procedure is repeated until no more cells in the immediate neighbourhood of cells which form the cluster exceed the fractional energy threshold. The threshold was chosen by optimising the energy resolution using a sample of 50 GeV single pointing photons. The same principle was employed to determine the energy weighted position of the shower in the first and back compartment, and a constraint was applied requiring that the position of the most energetic cell in the first and back compartment be near the vicinity of the most energetic cell in the middle compartment.

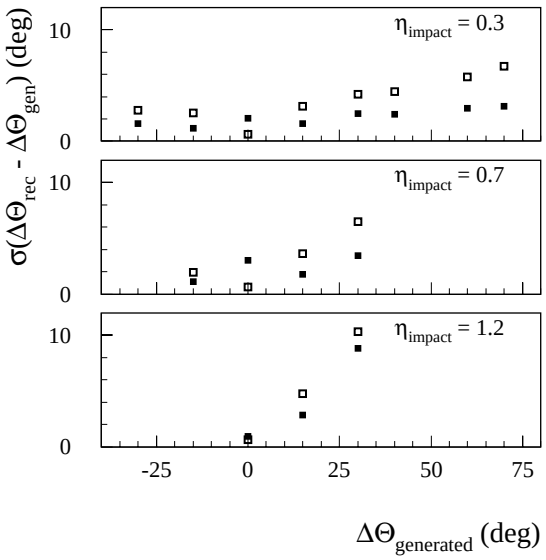

Figure 4-43 Angular resolution as a function of $\Delta\theta$, the deviation from pointing, for three different impact points in the EM Calorimeter. The open symbols show the results from the standard reconstruction, and the closed symbols show the results from the nearest neighbour clustering algorithm.

The angular measurement was made using the position information in the first and middle compartment only. The angular resolution obtained with this algorithm is shown superimposed to the standard reconstruction results in Figure 4-43. The performance of the nearest neighbour algorithm is much better than the standard reconstruction for the case of photons with large deviations from pointing. If S-shape corrections are included, the nearest neighbour algorithm provides results similar to the standard reconstruction for pointing photons and slightly better for non-pointing photons. This behaviour is expected, since the out-of-cluster showering is important for non-pointing objects in the case of fixed-cluster algorithms, whilst the nearest neighbour algorithm accounts for this effect.

In conclusion, the EM Calorimeter has a good capability to recognise and measure non-pointing photons. While the angular resolution with the standard reconstruction degrades for large deviations from pointing, preliminary investigations using neural networks and alternative clustering methods provide superior performance for non-pointing photons. As discussed in Section 20.3.2.4, the angular precision obtained so far is already sufficient to efficiently distinguish between non-pointing photons and pointing photons, providing excellent sensitivity to GMSB models. Further optimisation of the reconstruction techniques for non-pointing photons is in progress.

4.5 γ / π^0 separation

The EM Calorimeter must be able to efficiently reject isolated π^0, in order to extract a possible $H \rightarrow \gamma\gamma$ signal over the background. A π^0 rejection factor of about three, for a single-photon efficiency of 90%, is needed. The calorimeter performance and the algorithms used for γ/π^0 separation have been described in detail in [4-1]. Since the recent changes to the calorimeter design do not have a significant impact on this aspect of the performance, only a few additional studies and results are reported here. The effect of the electronic noise and pile-up at high luminosity has been checked with the complete simulation procedure described in Section 4.2.4. The results are summarised in Figure 4-44. For a fixed photon efficiency of 90%, the electronic noise and pile-up expected at high luminosity reduce the π^0 rejection by less than 10%.

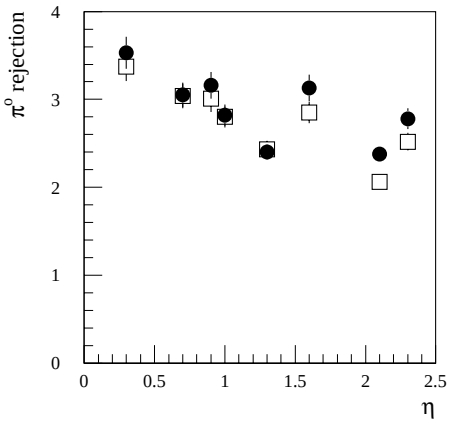

Figure 4-44 Rejection of π^0 of E_T = 50 GeV for 90% photon efficiency, as a function of pseudorapidity, with (open squares) and without (dots) including the electronic and pile-up noise expected at high luminosity.

Table 4-7 Rejection factors of π^0 of E_T = 50 GeV, as a function of the dispersion in the electrode alignment. Results are given at two pseudorapidity points and for 90% photon efficiency.

Dispersion	**0 μm**	**±400 μm**	**±1000 μm**
η = 0.3	3.53 ± 0.18	3.50 ± 0.17	3.35 ± 0.18
η = 1.0	2.89 ± 0.13	2.86 ± 0.12	2.77 ± 0.08

The impact of a possible cross-talk between adjacent strips in η has been evaluated. The results are shown in Figure 4-45. For a cross-talk of 10%, the π^0 rejection is degraded by about 10%. Recent results obtained from the beam test of module zero's indicate that the cross-talk between strips expected in ATLAS is of order 5%.

The impact of a non-perfect alignment of the kapton electrodes along the *z* direction (see Sections 4.4.2) has been studied, since a dispersion in the electrode position may affect the shower shape. The results are presented in Table 4-7. The rejection deteriorates by a few percent for very large misalignments (±1000 μm), because the shower appears to be broader, but is not affected for the expected dispersion of ±400 μm.

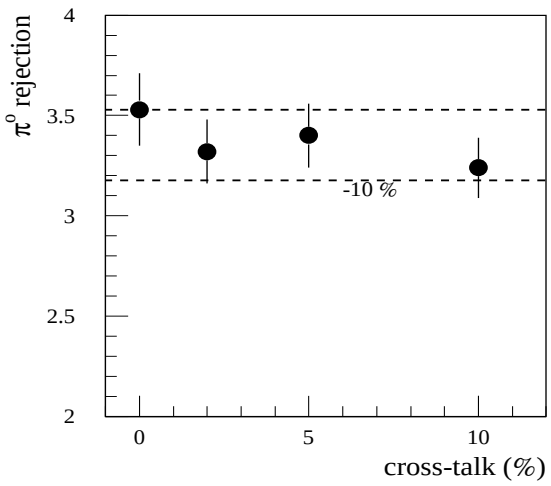

Figure 4-45 Rejection against π^0 of E_T = 50 GeV at η = 0.3, for 90% photon efficiency, as a function of the amount of cross-talk between adjacent strips.

4.6 Calorimeter performance and calibration with $Z \rightarrow ee$ events

The calorimeter performance, which has been illustrated in the previous sections using single particles, has also been studied with complete fully-simulated physics events, namely $Z \rightarrow ee$ decays. This channel has the advantage of being a simple, background-free, well-known process, and therefore ideal for benchmark performance studies in the LHC environment. Moreover, $Z \rightarrow ee$ decays are expected to be used to understand several aspects of the detector response, *e.g.* calibration of the absolute calorimeter scale, intercalibration of the calorimeter cells.

A sample of 50000 inclusive $Z \rightarrow ee$ events, which corresponds to an integrated luminosity of 0.07 fb^{-1}, has been generated by using PYTHIA interfaced to PHOTOS [4-15], in order to simulate single-photon emission and radiative decays. At the generation level, both electrons were required to have transverse momenta larger than 15 GeV and to be emitted at pseudorapidities $|\eta| < 2.5$. The generated sample was then processed with the ATLAS full simulation.

Several performance results obtained with these events are presented in Section 4.6.1, whereas the determination of the global constant term of the energy resolution is discussed in Section 4.6.2. At the LHC, $Z \rightarrow ee$ decays will also be used to determine the calorimeter absolute energy scale, as described in Chapter 12.

4.6.1 Calorimeter performance with $Z \rightarrow ee$ events

The main calorimeter performance issues have been studied with $Z \rightarrow ee$ events. These events are characterised by a realistic p_T spectrum of the electrons in the final state, by angular distributions covering more or less uniformly the full pseudorapidity acceptance of the calorimeter, and by the presence of an underlying activity from the spectator partons.

Electrons were required to have $E_T > 20$ GeV. Events containing a hard photon from internal bremsstrahlung were removed. Electronic noise and pile-up were not included.

The energy reconstructed in the calorimeter is shown in Figure 4-46 as a function of pseudorapidity, over the full calorimeter coverage. The calorimeter was calibrated in this simulation with single photons of $E_T = 50$ GeV incident at fixed pseudorapidity points. The energy of both electrons was then scaled up by 0.5%, in order to correct for the slightly different response to photons and electrons, arising from the material in front of the calorimeter.

The reconstructed energy spectrum is shown in Figure 4-47. The overall resolution is $11.4\% / \sqrt{E}$ and includes the contribution of the sampling term (averaged over pseudorapidity), of the constant term due to the calorimeter geometry (residual non-uniformities such as the ϕ-modulation) and of the underlying event. Electrons in the crack region $1.37 < |\eta| < 1.52$ were not considered. This result is in agreement with the single-particle resolution presented in Section 4.3.5.

About 80% of the events are contained inside a window of $\pm 2\sigma$ around the peak, where σ is the resolution shown in Figure 4-47. Additional information about the (mostly low-energy) tails is presented in Figure 4-48, which shows the pseudorapidity distribution for electrons outside the $\pm 2\sigma$ window. Excesses of events are visible in the regions of the cracks at $\eta \sim 0$, $|\eta| \sim 1.5$ and $|\eta| \sim 2.5$, where the resolution is degraded.

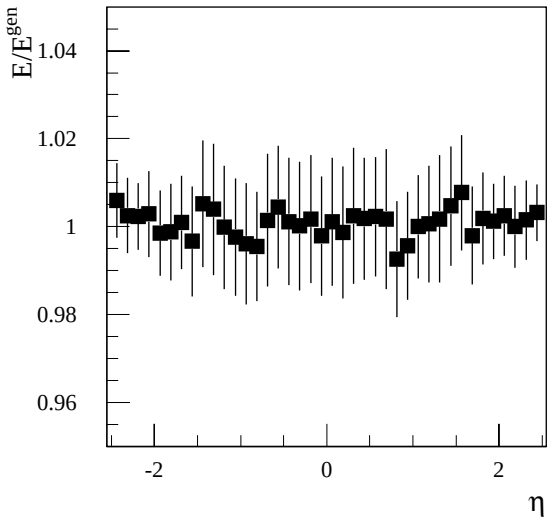

Figure 4-46 Reconstructed energy in the calorimeter, divided by the true energy, for electrons from Z decays as a function of pseudorapidity. The error bars give the rms spread on the reconstructed energy.

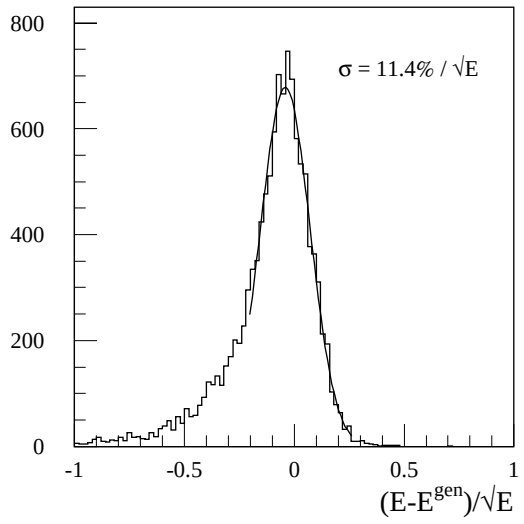

Figure 4-47 Difference between the reconstructed energy in the calorimeter and the true energy, divided by the square root of the true energy, as obtained for electrons from Z decays. The best fit is superimposed.

The position resolutions in ϕ and η are shown in Figures 4-49 and 4-50 respectively. The ϕ-resolution of the middle compartment is about 9.5 mrad / $\sqrt{E}$, the η-resolution of the strip section is about 2.7×10^{-3} / $\sqrt{E}$, and the η-resolution of the middle compartment is about 5.3×10^{-3} / $\sqrt{E}$. These results are in agreement with those obtained for single particles, presented in Section 4.4.1 and Section 4.4.2.

In conclusion, no deterioration of the performance is observed for complete physics event, as compared to single particles incident at fixed pseudorapidity points.

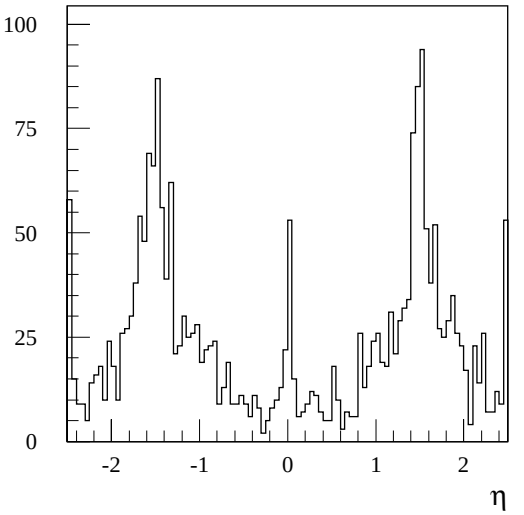

Figure 4-48 Distribution of the electron pseudorapidity for events which are at more than $\pm2\sigma$ from the peak of the distribution in Figure 4-47.

4.6.2 Calorimeter calibration and the global constant term

As discussed in Section 4.3.6, good uniformity of response of the EM Calorimeter will be provided, inside regions of size $\Delta\eta\times\Delta\phi = 0.2\times0.4$, by the electronic calibration system and by construction tolerances, which should guarantee a local constant term of 0.5% or smaller. Electron pairs from Z decays can then be used to intercalibrate the 440 regions of which the calorimeter is composed.

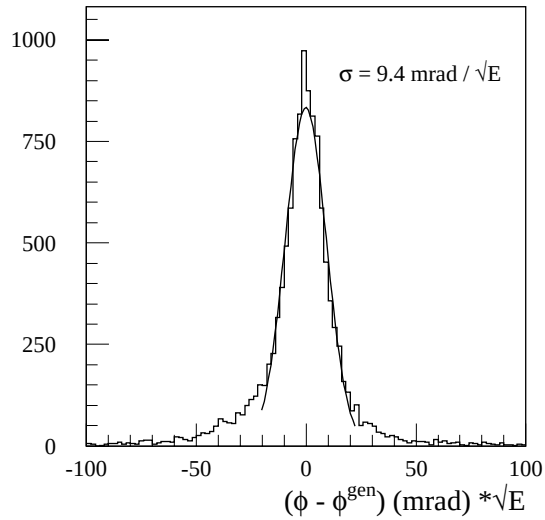

Figure 4-49 Difference between the reconstructed ϕ-position in the calorimeter and the true position, divided by the square root of the true energy, as obtained for electrons from Z decays. The best fit is superimposed.

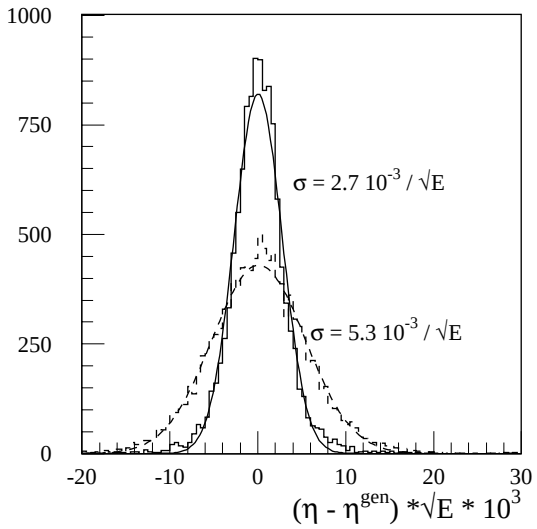

Figure 4-50 Difference between the reconstructed η-position in the calorimeter and the true position, divided by the square root of the true energy, as obtained for electrons from Z decays in the strip section (full histogram) and in the middle compartment (dashed histogram). The best fits are superimposed.

The advantages of using this process are:

- $Z \rightarrow ee$ decays occur at a very high rate, approximately 1 Hz at low luminosity.
- It is a clean channel, almost background free.
- Since the calibration is performed by imposing the *Z*-mass constraint, no information from other subdetectors is needed. Therefore $Z \rightarrow ee$ decays provide a mean of calibrating the EM Calorimeter in a standalone way. In this respect this method is complementary to measuring *E/p* for isolated electrons (Chapter 7), which is based on the momentum measurement in the Inner Detector.
- The *Z* resonance is close in mass to several particles which will be precisely measured or looked for, such as *W* bosons (see Chapter 16) and the low-mass Higgs boson (see Chapter 19).

The calibration is done by constraining the two-electron invariant mass to the *Z* mass.

The long–range non–uniformity of the calorimeter has been simulated by injecting random miscalibration coefficients (with an rms of 1.5%) in the 440 regions of size $\Delta\eta \times \Delta\phi = 0.2 \times 0.4$. These coefficients were then recovered by a log–likelihood fit of the reconstructed *Z* mass to the expected *Z* lineshape, which is shown in Figure 4-51.

Depending on whether the different compartments of the EM Calorimeter, *i.e.* the strip section and the middle compartment, are considered separately or not, there are 880 or 440 correction coefficients entering the fit (the back compartment is always added to the middle compartment). Simulations done at the particle level, with the correct energy smearing and energy fraction deposited in the strip section, show that for small Z samples (up to 50K events), it is better to use a 440-coefficient correction set, that is to calibrate by towers rather than by cells, even if the responses of the strip section and of the middle compartment fluctuate independently. Therefore the two compartments have not been distinguished in the study done with full simulation.

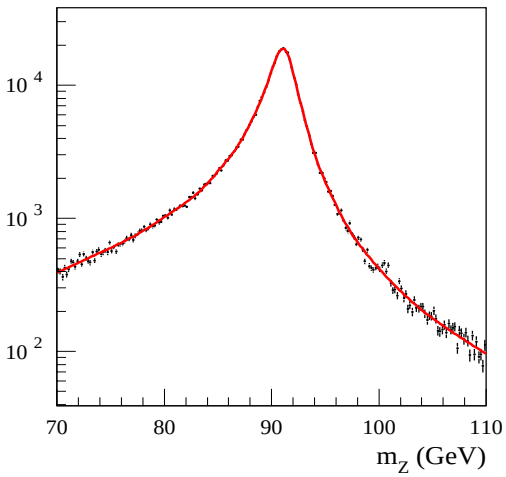

Figure 4-51 The Z lineshape as obtained from PYTHIA and PHOTOS.

Due to the fiducial cut $|\eta| < 2.5$ for both electrons, a few regions located close to the boundary had less than 25 electrons. Miscalibration (input) coefficients were injected also in these regions as in the rest of the calorimeter, but no fit was attempted. The calibration procedure was repeated ten times, each time with a different set of input coefficients. Figure 4-52 shows the correlation between the miscalibration (input) coefficients and the correction (output) coefficients.

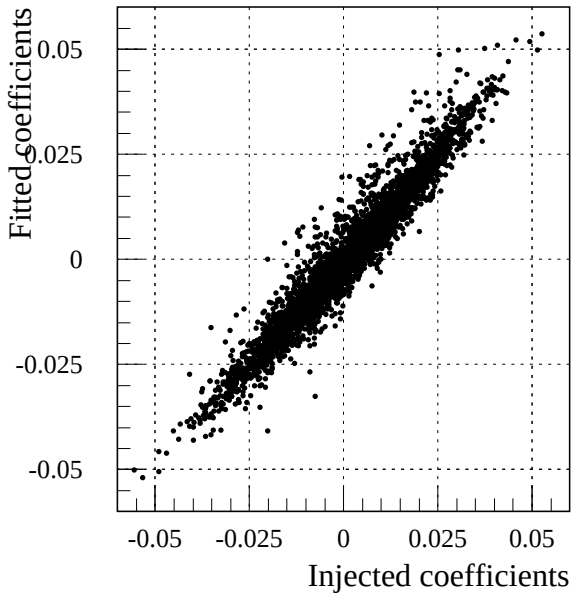

Figure 4-52 The fitted correction coefficients versus the injected coefficients, as obtained for $Z \rightarrow ee$ events.

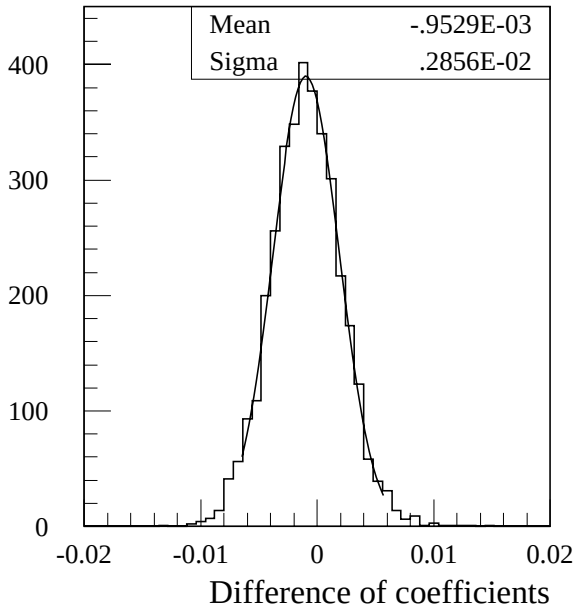

Figure 4-53 The difference between the injected coefficients and the correction coefficients after the fit.

The resulting uniformity after the calibration procedure is shown in Figure 4-53 for regions with at least 60 incident electrons. Regions located near the crack at $\eta = 1.5$ are excluded. After the fit, the rms non-uniformity (*i.e.* the global constant term) has been reduced from 1.5% to less than 0.3%. The *Z* sample used in this example will be collected in less than 48 hours of data taking at low luminosity. Therefore, by summing the local constant term of 0.5% (Section 4.3.6) with the global constant term of 0.3% obtained as described here, a total constant term of about 0.6% should be achieved in a few days of data taking. This is well within the goal of 0.7%.

Several checks have been made of the stability of this procedure, given the large number of unknowns and possible strong correlations between coefficients. For instance, the reconstructed *Z* mass can be corrected by using only one of the two regions involved. In this respect, the transverse momentum of the *Z* is essential to stabilise the system of equations. Without some acoplanar e^+e^- pairs, only regions which are back-to-back in ϕ would be involved, leading to non-unique solutions of the system. However, only a small fraction (~1%) of events with acoplanar electron pairs is sufficient to remove such ambiguities. A test was also made, which consisted in injecting a large offset of 6% over the whole upper half of the calorimeter ($0° < \phi < 180°$) in addition to the 1.5% non-uniformity. The fit converged without problems.

4.7 Performance of module zero's

After a rather long period of prototype activities (1990 to 1996), which addressed the detector's mechanical structure, the choice between a presampler and a preshower, and the development of the front-end electronics, the construction of module zero's was launched in 1996-1997.

Module zero's have exactly the same dimensions and structure as the detector modules. Their construction is intended to be a final qualification of all fabrication processes, and a last assessment of the performance. In order to be as close as possible to the ATLAS conditions, motherboards, cold cables, feedthroughs, crates and back-planes, which connect a given calorimeter cell to its electronic circuit on the front-end boards, and the electronic circuit itself, were built according to the final design (radiation hardness of the various circuits was the only exception). The absorbers and support fixtures were built with the final tooling and Quality Control procedure. Detailed mechanical measurements have shown that all tolerances meet the specifications [4-16].

On the other hand, the construction of the readout electrodes presented some difficulties, which resulted in significant delays. Therefore, in order to be ready for the beam tests in 1998, the endcap module contained only 15 electrodes instead of the foreseen 128, and the barrel module 23 electrodes instead of 128. This allowed studies of the local performance to be made, but did not permit a test of the uniformity of the calorimeter response over a large area.

The module zero of the barrel presampler, which consisted of two sectors, was complete.

The electronic calibration of both the calorimeter and the presampler modules was made using prototypes of the 128-channel calibration boards designed for ATLAS. The uniformity of the delivered signals, shown in Figure 4-25, is 0.2% rms, which meets the requirement of 0.25%. Checks are going on to ensure that this uniformity is preserved at the level of the current pulses generated close to the calorimeter cell.

The front-end readout boards (128 channels) used in the test of the module zero's have all the final functionalities. Each channel consists of a preamplifier, a three-gain shaper, and for each gain a 144 cell-deep analog memory (SCA) in which samples of the signals taken every 25 ns are stored. Digitisation is performed using 12 bits. Calibration and test-beam data were processed using five samples around the maximum. Using these five samples and the optimal-filtering technique, all beam events could be used, irrespective of their exact arrival time with respect to the 40 MHz clock of the SCA. The set-up also allowed to record continuous waveforms of both beam and calibration events, which proved extremely useful for the detailed understanding of the signal behaviour (presence of inductive effects, cross-talk, *etc.*).

The system-aspect information and the data gathered during the beam tests and their preparation are very valuable and allow the last details to be frozen before the detector production starts. Preliminary results from the beam tests are discussed in the next sections.

4.7.1 The barrel module zero

The barrel module was tested with 20 GeV electrons, obtained from a lead-ion beam. The energy reconstructed in the calorimeter at one of the beam impact positions, which corresponds to $\eta = 0.3$, is shown in Figure 4-54. Despite that cuts were applied to suppress pions in the beam, a small fraction of them remain in the low-energy tail. The energy resolution measured after the subtraction of the electronic noise is $10.0\% / \sqrt{E}$. This is somewhat worse than the performance expected at this pseudorapidity (see Figure 4-20). Likely explanations are the contribution of the beam spread, which was not subtracted, and the fact that the best possible calibration was not used in obtaining these preliminary results.

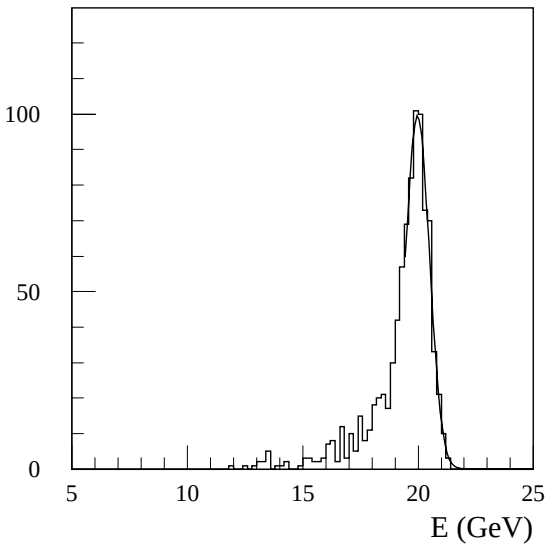

Figure 4-54 Energy spectrum reconstructed in the barrel module zero for 20 GeV electrons at $\eta = 0.3$. A 5x4 cell cluster in $\eta x \phi$ has been used.

The noise levels per cell, 18 MeV in the strip section, 47 MeV in the middle compartment and 35 MeV in the back compartment, are slightly better (15%) than expected. The measured sensitivity is 2.6 μA / GeV, to be compared to the expected 2.74 μA / GeV.

4.7.2 The end-cap module zero

In the past a prototype with a variable thickness of the lead plates had been tested [4-17], therefore this was the first time that an end-cap module with the final geometry (constant thickness of the lead plates) was exposed to beam.

Since the module was only partially equipped with readout electrodes, it was not possible to perform complete azimuthal scans to look at the response uniformity. However, the calorimeter energy resolution could be measured at two pseudorapidity positions ($\eta \sim 1.55$ and $\eta \sim 2.2$). Electron beams in the energy range 20 to 200 GeV were used for this measurement.

The reconstructed energy spectrum for electrons of energy 150 GeV at $\eta \sim 2.2$ is shown in Figure 4-55. The low-energy tails are due to the poor quality of the beam. The resolution is about 1%.

Figure 4-56 shows the calorimeter energy resolution as a function of the incident beam energy. At each energy point, the beam spread as well as the electronic noise (see below) were subtracted in quadrature. The local constant term of $0.42 \pm 0.05\%$ is somewhat higher than expected (0.3%). It is, however, good enough given that results are preliminary.

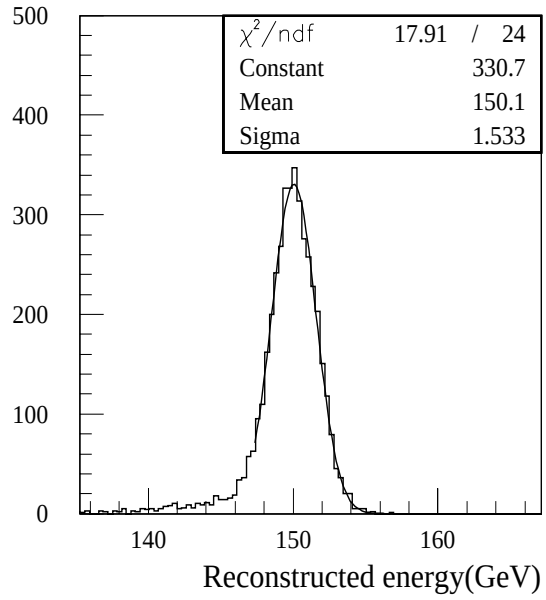

Figure 4-55 Energy spectrum reconstructed in the end-cap module zero for electrons of energy 150 GeV at $\eta \sim 2.2$.

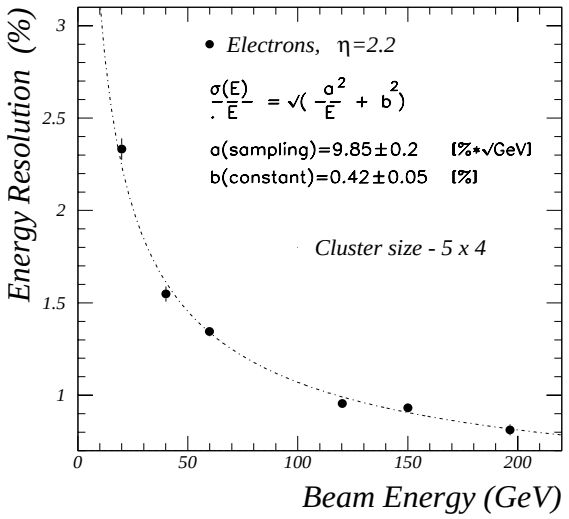

Figure 4-56 Energy resolution of the end-cap module zero as a function of energy at $\eta \sim 2.2$. The best fit (see text) is superimposed.

These measurements were done with two different gains of the electronic chain: high gain up to 60 GeV and medium gain above 60 GeV. This results in different values of the electronic noise for the two groups of runs. Since the number of energy points was limited, instead of obtaining the electronic noise in a given cluster from the fit to the energy resolution curve, the noise levels were directly measured in random-trigger events.The observed noise per channel is of the order of 20 MeV in the strip section and 50 MeV in the middle compartment, in agreement with the expectation. The cross-talk observed between the middle and back compartment of the calorimeter (~3%) is larger than expected, and has been attributed to the motherboard design. The linearity of the calorimeter energy response, shown in Figure 4-57, is well within 1%.

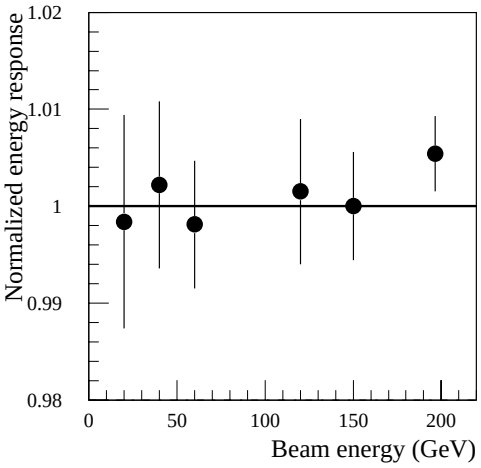

Figure 4-57 Mean energy response of the end-cap module zero as a function of the beam energy at $\eta = 2.2$.

In conclusion, apart from the overall uniformity of the calorimeter, which will be measured in the future with modules fully equipped with readout electrodes, and apart from some problems (noise, cross-talk) which have been understood and will be cured, the results obtained so far from the beam tests of the EM module zero's indicated that the detector performance meets the requirements.

4.8 Conclusions

An extensive optimisation work over the past years has led to the design of an electromagnetic calorimeter which offers good energy resolution, excellent response uniformity and angular resolution, and powerful particle identification capability.

The main performance issues presented in this chapter, which are based on a full detailed simulation of the accordion geometry within the rest of the ATLAS detector, can be summarised as follows. The sampling term of the energy resolution is at the level of $10\%/\sqrt{E}$. Owing to the intrinsic uniformity of the liquid-argon technique, and to strict construction tolerances, a global constant term of less than 0.7% should be achieved in a few days of data taking at low luminosity using $Z \rightarrow ee$ events. At high luminosity, the total energy resolution for photons of E_T = 50 GeV is 1.6% or better.

By using the fine longitudinal and lateral segmentation, several precision measurements of the shower position and angle can be performed. In particular, the primary vertex in $H \rightarrow \gamma\gamma$ events can be measured with an accuracy of 1.3 cm by using the calorimeter information alone, and high sensitivity should be achieved for new physics characterised by the presence of photons not coming from the primary vertex.

An average rejection factor of three against π^0 should be obtained for a photon efficiency of 90%. More examples of particle identification issues, involving the use of the EM Calorimeter, the Inner Detector and the Hadronic Calorimeters, can be found in Chapters 7 and 9.

With respect to the studies reported in the Calorimeter Performance TDR, the results presented here are based on a more realistic simulation and deeper understanding of several effects. In particular, the impact on the performance coming from a more correct treatment of the pile-up and from several imperfections in the mechanics and electronics (cross-talk, electrode alignment, non-uniformity of the electric field, *etc.*) was evaluated.

Finally, preliminary results from the beam tests of module zero's indicate that the performance of the detector which is being built is in agreement with the physics requirements and the expectations from the simulation.

4.9 References

4-1 ATLAS Collaboration, Calorimeter Performance Technical Design Report, CERN / LHCC 96-40 (1996).

4-2 ATLAS Collaboration, Liquid Argon Calorimeter Technical Design Report, CERN / LHCC 96-41 (1996).

4-3 Y. Jacquier *et al.*, 'Strengths and weaknesses of digital filtering', ATLAS Internal Note ATL-LARG-97- 80 (1997).

4-4 G. Le Meur and F. Touze, 'PRIAM / ANTIGONE: a 2D / 3D package for accelerator design', in Proceedings of the 2nd European Particle Accelerator Conference, London 1993, p1321-1323.

4-5 ATLAS Collaboration, Technical Proposal, CERN / LHCC 94-43 (1994).

4-6 RD3 Collaboration, Nucl. Instr. Meth. **A364** (1995) 290.

4-7 M.-L. Andrieux *et al.*, 'Pollution of liquid argon after neutron irradiation measured at SARA: summary of raw data', ATLAS Internal Note ATL-LARG-98-105 (1998).

4-8 L. Poggioli, 'The LARG Slow Control. Status Report', ATLAS Internal Note ATL-LARG-98-110 (1998).

4-9 B. Canton *et al.*, 'Analysis and results of the measurements of the plate thickness, done at the factory, during the production of the lead for the module zero of the barrel and end-cap ATLAS Electromagnetic Calorimeter', ATLAS Internal Note ATL-LARG-97-76 (1997).

4-10 B. Mansoulie, 'Non-uniformity of lead plates and gaps: analytical estimates of the shower averaging effect', ATLAS Internal Note ATL-LARG-98-99 (1998).

4-11 W. Bonivento *et al.*, 'Cold cables for the EM Calorimeters: specifications and measurements of the electrical properties', ATLAS Internal Note ATL-LARG-98-106 (1998).

4-12 A. Ferrari and J. Soderqvist, 'A study of the presampler intersector crack', ATLAS Internal Note ATL-LARG-97-084 (1997).

4-13 J. Schwindling, 'S-shape correction using a neural network', ATLAS Internal Note ATL-LARG-98-104 (1998).

4-14 L. Borissov *et al.*, 'Study of non-pointing photon signatures of Gauge-Mediated SUSY-Breaking models', ATLAS Internal Note ATL-PHYS-99-37 (1999).

4-15 Z. Was *et al.*, Comput. Phys. Commun. **79** (1994) 291.

4-16 L. Labarga and P. Romero, 'Analysis of the quality control measurements performed on the absorbers produced for the module zero of the ATLAS Electromagnetic end-cap Calorimeter', ATLAS Internal Note ATL-LARG-99-004 (1999).

4-17 RD3 Collaboration, Nucl. Instr. Meth. **A389** (1997) 398.